The Impact of Assimilating Z_{DR} Observations on Storm-Scale Ensemble Forecasts of the 31 May 2013 Oklahoma Storm Event

BRYAN J. PUTNAM,[a] YOUNGSUN JUNG,[a,b] NUSRAT YUSSOUF,[b,c,d] DEREK STRATMAN,[c,d] TIMOTHY A. SUPINIE,[a,b] MING XUE,[a,b] CHARLES KUSTER,[c,d] AND JONATHAN LABRIOLA[a,b]

[a] *Center for Analysis and Prediction of Storms, University of Oklahoma, Norman, Oklahoma*
[b] *School of Meteorology, University of Oklahoma, Norman, Oklahoma*
[c] *Cooperative Institute for Mesoscale Meteorology Studies, University of Oklahoma, Norman, Oklahoma*
[d] *NOAA/OAR/National Severe Storms Laboratory, Norman, Oklahoma*

(Manuscript received 11 August 2020, in final form 2 March 2021)

ABSTRACT: Assimilation of dual-polarization (dual-pol) observations provides more accurate storm-scale analyses to initialize forecasts of severe convective thunderstorms. This study investigates the impact assimilating experimental sector-scan dual-pol observations has on storm-scale ensemble forecasts and how this impact changes over different data assimilation (DA) windows using the ensemble Kalman filter (EnKF). Ensemble forecasts are initialized after 30, 45, and 60 min of DA for two sets of experiments that assimilate either reflectivity and radial velocity only (EXPZ) or reflectivity and radial velocity plus differential reflectivity (EXPZZDR). This study uses the 31 May 2013 Oklahoma event, which included multiple storms that produced tornadoes and severe hail, with a focus on two storms that impacted El Reno and Stillwater during the event. The earliest initialized forecast of EXPZZDR better predicts the evolution of the El Reno storm than EXPZ, but the two sets of experiments become similar at subsequent forecast times. However, the later EXPZZDR forecasts of the Stillwater storm, which organized toward the end of the DA window, produce improved results compared to EXPZ, in which the storm is less intense and weakens. Evaluation of forecast products for supercell mesocyclones [updraft helicity (UH)] and hail show similar results, with earlier EXPZZDR forecasts better predicting the UH swaths of the El Reno storm and later forecasts producing improved UH and hail swaths for the Stillwater storm. The results indicate that the assimilation of Z_{DR} over fewer DA cycles can produce improved forecasts when DA windows sufficiently cover storms during their initial development and organization.

KEYWORDS: Severe storms; Cloud microphysics; Radars/Radar observations; Ensembles; Numerical weather prediction/forecasting; Data assimilation

1. Introduction and motivation

Many significant advancements have been made over the recent decades in storm-scale data assimilation (DA) and forecasting, including, but not limited to, the initial concept paper of Lilly (1990), the establishment of a 10-yr National Science Foundation Science and Technology Center (Droegemeier 1990), and in more recent years the establishment of the NOAA Warn-on-Forecast (WoF) program (Stensrud et al. 2009, 2013). Notable advancements have also been made in convection-allowing operational forecasting systems such as the Rapid Refresh (RAP; Benjamin et al. 2016) and High-Resolution Rapid Refresh (HRRR; Alexander et al. 2020). Under the WoF vision, forecasts of various hazards produced by severe thunderstorms (e.g., hail, flash flooding, and tornadoes) would provide guidance to operational meteorologists to use when issuing warnings. Therefore, a principal goal of WoF is to increase warning lead times compared to those currently issued, which are mainly based on observations of hazards already occurring or of their precursors. The WoF system forecasts will use increasingly higher-resolution numerical models needed to represent convective-scale processes (Bryan et al. 2003) in combination with sophisticated parameterization schemes and will assimilate high-resolution, high-frequency radar, satellite, and conventional (e.g., surface observations and radiosondes) observations using advanced DA methods while providing more frequently updated forecasts. Furthermore, the WoF system will be ensemble based so that the system can encapsulate forecast uncertainties to provide probabilistic guidance.

One of the important goals of the WoF system is to generate forecast initial conditions (also known as analyses) rapidly using observations collected over as short a time period as possible while being able to accurately estimate the internal states of convective storms, including the cloud microphysics (Stensrud et al. 2013). Dual-polarization (dual-pol) radar measurements became valuable new sources of observational information on precipitating systems when the U.S. operational WSR-88D network was upgraded to dual-pol capabilities (Radar Operations Center 2013). Meanwhile, phased-array radar (PAR) technologies with dual-pol capability are being developed as the next generation operational weather surveillance radar to replace the aging WSR-88D network (Lei et al. 2007; Yussouf and Stensrud 2010; Supinie et al. 2017;

Putnam's current affiliation: NOAA/NWS/NCEP Weather Prediction Center, College Park, Maryland.

Jung's current affiliation: NOAA/NWS Office of Science and Technology Integration, Silver Spring, Maryland.

Corresponding author: Ming Xue, mxue@ou.edu

DOI: 10.1175/MWR-D-20-0261.1

Weber et al. 2017; Stratman et al. 2020). PAR is able to provide much more frequent volume scans (~2 min) of the atmosphere by focusing on certain storms using sector scans instead of completing a full 360° rotation like the current WSR-88D network (~5 min). Additionally, there have been many real storm case studies that use advanced model microphysics schemes and DA methods, such as the ensemble Kalman filter (EnKF; Evensen 1994, 2003), that have shown promising results in improving storm-scale forecasts (e.g., Snook et al. 2012; Yussouf et al. 2016; Supinie et al. 2017; Skinner et al. 2018; Labriola et al. 2019a; Putnam et al. 2019; Snook et al. 2019). The advancements in these areas are vital to representing the highly complex nonlinear microphysical and dynamical processes in convective storms that are intrinsically linked to dual-pol radar measurements. The availability of dual-pol observations and advancements in DA methods provide the tools necessary to better investigate the impact dual-pol observations have on providing improved, accelerated creation of initial conditions for storm-scale ensemble forecasts to further advance WoF capabilities (Putnam et al. 2014; Wheatley et al. 2015; Putnam et al. 2017; Skinner et al. 2018; Putnam et al. 2019).

Dual-pol observations provide more insights on the microphysical state of convective storms than the single-polarization radar reflectivity (Z) and radial velocity (V_r) observations can. For example, differential reflectivity (Z_{DR}) contains information on the size of hydrometeors by comparing the reflectivities of horizontal and vertical polarizations (Z_H and Z_V; Bringi and Chandrasekar 2001). Larger Z_{DR}, corresponding to larger Z_H compared to Z_V, is associated with raindrops that grow more oblate as they increase in size. Thus, Z_{DR} provides a second independent observation of the microphysical state and additional information to adjust the particle size distributions (PSDs) associated with multimoment microphysics schemes through DA (Putnam et al. 2019). A double-moment (DM) microphysics scheme allows for the determination of two independent parameters of PSDs (Milbrandt and Yau 2005), which need to be initialized for the forecast. The Z and Z_{DR} observations together allow for more physical estimation of the hydrometeor PSDs, which in DM schemes are commonly expressed in terms of mass mixing ratio (q) and total number concentrations (N_t) for each species (e.g., Milbrandt and Yao 2005; Morrison et al. 2005; Thompson et al. 2008; Morrison et al. 2009; Lim and Hong 2010; Mansell et al. 2010).

Studies have shown that multimoment microphysics schemes lead to better analyses and forecasts, including better handling of the important process of size sorting (Jung et al. 2012; Dawson et al. 2014; Putnam et al. 2014; Wheatley et al. 2014; Putnam et al. 2017, 2019). Certain patterns of Z_{DR} observations have been identified among other polarimetric signatures that reveal important microphysical and dynamical processes in convective storms (Balakrishnan and Zrnić 1990; Zrnić et al. 1993; Brandes et al. 1995; Zrnić and Ryzhkov 1999; Loney et al. 2002; Scharfenberg et al. 2005; Kumjian and Ryzhkov 2008; Van Den Broeke et al. 2008; Snyder et al. 2013; Dawson et al. 2014; Kumjian et al. 2014; Tanamachi and Heinselman 2016; Carr et al. 2017; Starzec et al. 2017; Van Den Broeke 2017; Kingfield and Picca 2018; Lim et al. 2018; Wu et al. 2018; Matsui et al. 2020; Van Den Broeke 2020). Examples include higher values of Z_{DR} at low levels along the right forward flank of supercells, in the form of a Z_{DR} arc, that are indicative of hail and rain size sorting aloft, while a vertical column of high Z_{DR} values above the melting layer due to suspended supercooled rainwater is indicative of the presence of a strong updraft, commonly referred to as the Z_{DR} column.

Dual-pol observations have been the subject of a number of real case DA studies that assess the impact of the data on model state estimation and subsequent forecasts. The studies of Wu et al. (2000) and Li and Mecikalski (2010, 2012), using various approaches to assimilate preretrieved hydrometeor mixing ratios from polarimetric observations, showed short-term forecast improvements in convective storm structure and location, although Wu et al. (2000) found that improvements did not last long into the forecasts. Li et al. (2017) showed that assimilating specific differential phase (K_{DP}) using a single-moment (SM) microphysics (MP) scheme helped improve analyses of rainwater and snow content in a mesoscale convective system. Yokota et al. (2016) assimilated V_r as well as rainwater content derived from Z and K_{DP} for a supercell storm and obtained improved prediction of the low-level mesocyclone within the supercell. Carlin et al. (2017) demonstrated that limiting the adjustments to the moisture and temperature fields within a cloud analysis procedure to locations of the Z_{DR} column improved forecasts of tornadic supercell updraft helicity and rotation tracks. The methods used above are all indirect methods where certain state variables are first derived from the observed quantities during assimilation. They differ in how the model state variables are updated but are similar in that not all state variables are updated because of the lack of cross covariance among the observed quantities and the state variables, and the final analyses are thus subject to gross imbalance.

While several studies investigated the impact of assimilating dual-pol observations on forecasts, they did not use advanced multimoment microphysics schemes needed to reproduce proper polarimetric signatures (e.g., Putnam et al. 2014; Dawson et al. 2014). Putnam et al. (2019) assimilated Z_{DR} observations directly using EnKF together with a DM microphysics scheme and found that the Z_{DR} assimilation improved analyzed rain and hail PSDs within a supercell, but no free forecast was considered. In this study, we expand upon the work of Putnam et al. (2019) and assess the impact of assimilating dual-pol observations on storm-scale forecasts using the same 5-min DA cycles as in Putnam et al. (2019) to facilitate direct comparisons. Apart from assessing the impact of dual-pol observations on subsequent forecasts, we also want to consider when and how many DA cycles covering the storm evolution are needed to achieve significant impacts on these forecasts. Toward this goal, we launch forecasts after 30, 45, and 60 min of DA and compare forecast performance. This serves to provide insight on how the addition of dual-pol observations may alter the length of the DA window necessary to produce adequate analyses to initialize forecasts. Further study may then further examine the impact of assimilating rapid-scan dual-pol observations based on the number of DA cycles required to achieve significant forecast impacts. The 31 May 2013

Oklahoma storm event, which included multiple supercell storms that produced tornadoes, hail, and widespread flash flooding, serves as an example case where storm-scale probabilistic forecasts would provide guidance in the warning process and better prepare the public for widespread and deadly storms.

We first present a brief overview of the 31 May 2013 storm event in section 2, including the atmospheric conditions that produced the storms, their complex evolution, and their subsequent impact on the Oklahoma City, Oklahoma, metropolitan area. Second, the experiment settings and methodology are outlined in section 3 by providing details on the experiment time line and domain, the processing of radar observations used, and the various settings for the EnKF DA method and forecast model used to produce staggered ensemble forecasts of the event. Next, the ensemble forecasts are evaluated in section 4 by comparing their structure, evolution, and progression; the forecast hazards they produce; and the various microphysical and dynamical states of the storms that contribute to these differences. Finally, conclusions are given together with thoughts and suggestions for future work in section 5.

2. Summary of the 31 May 2013 Oklahoma storm event

A prolonged series of supercell thunderstorms occurred over central and northern Oklahoma during the afternoon and evening of 31 May 2013. These storms were associated with the latest in a series of upper-level troughs that led to multiple significant severe weather outbreaks over the plains in late May 2013. A strong surface low pressure center (~990 hPa) was located over the eastern Dakotas. A stationary front trailed to the south-southwest and passed over northern Oklahoma where there was a secondary, weaker low pressure center with an associated southwesterly-oriented dryline. These boundaries along with the southeasterly flow ahead of the low pressure center led to a region of enhanced convergence. Rich, deep gulf moisture was already in place from the previous storm systems and was readily accessible given the late spring timing. Surface dewpoints of 70°–73°F (21°–23°C) and the cold air aloft associated with the upper-level trough led to extreme CAPE values in excess of 5000 J kg^{-1} (SPC 2019).

An initially stout cap was breached due to continued moisture advection, increasing CAPE, and convergence along the stationary front and near the dryline–stationary front triple point after 2100 UTC; numerous storms quickly developed. The storms included an explosive supercell that produced an EF-3 tornado near El Reno, Oklahoma, that initiated near the triple point and at the southern end of a line of additional thunderstorms developing along the stationary front. This tornado killed 8 people and was followed by several short-lived tornadoes across the Oklahoma City metropolitan area. New storms continued to develop near the stalled triple point due to the convergence and continued moisture advection and move east over Oklahoma City. Several hours of training thunderstorms and torrential rainfall led to prolonged and widespread flash flooding that killed an additional 14 people (NWS 2019).

3. Experiment methods and settings

a. Experiment domain and time line

The experiment domain as well as the background forecast and boundary conditions for the dual-pol DA experiments use the multiscale DA and forecast setup of Stratman et al. (2020) and are summarized in Fig. 1. There are three experiment domains with 36 ensemble members that are consecutively nested for each member. The prediction model used for forecasts on each domain is the Advanced Research version of the Weather Research and Forecasting (WRF-ARW) Model (version 3.9.1.1; Skamarock et al. 2008). The ensemble for the first, outermost domain is created by interpolating the first 18 ensemble members of the National Centers for Environmental Prediction's (NCEP) Global Ensemble Forecast System (GEFS; NOAA/NCEP 1992; Toth et al. 2004; Wei et al. 2008) to a grid with 15-km horizonal grid spacing that covers the CONUS. The GEFS members are used twice to generate ensemble members 1 through 18 (GEFS members in order) and 19 through 36 (GEFS members in reverse order) and use different physics combinations following Table 2 of Yussouf et al. (2015). The physics combinations include the Kain–Fritsch (Kain and Fritsch 1993; Kain 2004), Grell-3 (Grell and Devenyi 2002), and Tiedtke (Tiedtke 1989; Zhang et al. 2011) cumulus parameterization schemes; the Yonsei University (YSU; Hong et al. 2006), Mellor–Yamada–Janjić (MYJ; Janjić 2002), and Mellor–Yamada–Nakanishi–Niino level 2.5 (MYNN2.5, Nakanishi and Niino 2006, 2009) planetary boundary layer (PBL) schemes; the Dudhia (Dudhia 1989) and RRTMG (Iacono et al. 2008) shortwave (SW) radiation schemes; and the RRTM (Mlawer et al. 1997) and RRTMG (Iacono et al. 2008) longwave (LW) radiation schemes. The members are then interpolated to a convection allowing 3-km grid that uses the same physics combinations as the 15-km grid except for omission of the cumulus parameterization. All members on both the 15-km and 3-km grid use the National Severe Storm Laboratory (NSSL) DM microphysics scheme (Mansell et al. 2010) and Noah land surface scheme (Tewari et al. 2004).

Forecasts are initialized at 0000 UTC 31 May 2013 for both the 15-km and 3-km ensembles, with the 15-km ensemble providing updated boundary conditions for the 3-km ensemble every hour through 0100 UTC 1 June 2013. Conventional observations are assimilated every hour on both grids using the EnKF algorithm (version 1.0; Hu et al. 2015b) implemented in the Gridpoint Statistical Interpolation system (GSI, version 3.4; Hu et al. 2015a). These include temperature and wind information from surface Automatic Surface Observing System (ASOS) and Automatic Weather Observing System (AWOS) stations as well as radiosondes (NOAA/NCEI 1901a,b, 1905). The 3-km grid is further interpolated to a 1-km grid at 2100 UTC 31 May 2013 that uses the same physics parameterizations as the 15- and 3-km grids. After a 1-h spinup forecast beginning at 2100 UTC, 5-min DA cycling begins at 2200 UTC and continues through 2300 UTC, or approximately 3 min before the start of the El Reno tornado noted in section 2 (Fig. 1d). The model forecast time steps 60 s for the 15-km grid, 12 s for the 3-km grid, and 3 s on the 1-km grid. In addition to the radar observations, conventional observations from the

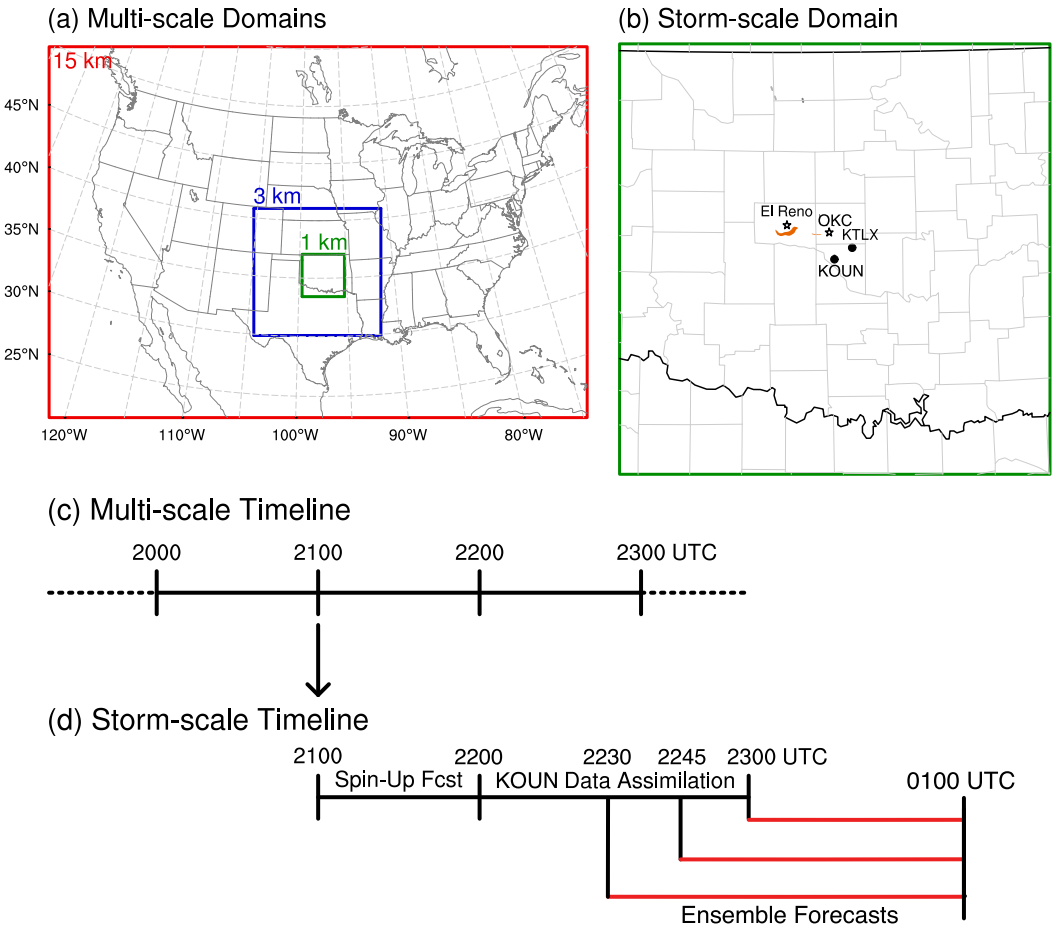

FIG. 1. Diagram of the (a) 15-km first outer domain, the 3-km second outer domain, and 1-km storm-scale experimental domain; (b) zoomed-in version of the 1-km storm-scale experimental domain with noted radars and locations of interest; (c) time line of the multiscale 15-km and 3-km outer domain forecasts; and (d) time line of the 1-km spinup forecast, the KOUN data assimilation period, and the staggered ensemble forecasts [adapted from Stratman et al. (2020)].

Oklahoma Mesonet (Oklahoma Climatological Survey/Oklahoma Mesonet 1994; Brock et al. 1995; McPherson et al. 2007) are assimilated on this grid as well. The closest conventional observation data in time to the DA cycle are assimilated while the closest KOUN sector-scan observation volume in time that begins before a given DA cycle is assimilated. This makes certain that the radar observations overlap the DA cycle and that there is no more than 2 min of difference in time between a radar observation and the DA cycle. The observations from the 2-min sector scans that do not overlap the 5-min DA cycles are not assimilated. Further details of the data assimilation and EnKF settings for the 1-km grid are given in section 3c.

To assess if assimilating the dual-pol observations reduces the number of cycles required to produce a reasonable forecast, three separate ensemble forecasts are initialized in each of two DA experiments: one assimilating Z and V_r (EXPZ) and one assimilating Z_{DR} in addition to Z and V_r (EXPZZDR). For each experiment, one forecast is initialized after 30 min of DA by the analysis at 2230 UTC, one after 45 min at 2245 UTC, and another after a more typical 1-h DA window for storm-scale DA experiments at 2300 UTC. Previous studies have shown assimilating 10–12 radar volumes of Z and V_r observations, or up to 1 h of DA for 5-min DA cycles, is necessary to accurately analyze the storms (Xue et al. 2006; Yussouf and Stensrud 2010). Experiments are named based on forecast initialization times (Table 1). The forecast from the 3-km grid provides updated boundary conditions every hour throughout the 1-km grid DA and forecast period. The time line of the forecasts on the outer 15- and 3-km domains as well as for the assimilation period and forecasts initialized from the 1-km grid is featured in Fig. 1.

b. *Radar observation preprocessing*

The NSSL's experimental dual-pol WSR-88D (KOUN; Ryzhkov et al. 2005; Scharfenberg et al. 2005) scanned the 31 May 2013 storm using sector scans to provide more rapid updates (~2-min volumes) while observing convective storms of interest (Kuster et al. 2017, 2019). The sectors in this case cover approximately 110° and shift from the west-northwest to

TABLE 1. Experiment names based on the observations assimilated and forecast initialization time.

Forecast initialization time	$Z + V_r$ DA expt	$Z + Z_{DR} + V_r$ DA expt
2230 UTC (30-min DA)	EXPZ_2230	EXPZZDR_2230
2245 UTC (45-min DA)	EXPZ_2245	EXPZZDR_2245
2300 UTC (60-min DA)	EXPZ_2300	EXPZZDR_2300

north over the event period following the movement of the mesocyclone of the El Reno–Oklahoma City tornadic supercell discussed in section 2. KOUN has the same 250 m gate spacing as the current WSR-88D network. These sector scans provide a focus on the storms of interest and serve as a proxy for a future upgraded dual-pol PAR observation network.

Several preprocessing steps were used on the raw KOUN observations. First, the NSSL's and Cooperative Institute for Mesoscale Meteorology Study's (CIMMS) Warning Decision Support System–Integrated Information (WDSS-II; Lakshmanan et al. 2007) program was used to provide quality control of the Z observations by removing spurious radar echoes due to ground clutter/biological scatterers identified via a hydrometeor classification algorithm that uses the available dual-pol observations (Lakshmanan et al. 2007, 2014). The Z and Z_{DR} observations are marked as missing where these Z observations have been identified as clutter/biological scatterers. The velocity observations were automatically dealiased by WDSS-II. The Z_{DR} calibration was performed using the presence of dry snow above the environmental melting layer in a manner similar to the method presented in Picca and Ryzhkov (2012). Due to errors during data acquisition, there are a few elevation scans where the velocity data are incomplete and contain anomalous values. These individual elevation scans are marked as missing, and no data are assimilated at those levels. The observations are interpolated on to the horizontal model grid points but left at the height of the radar tilt elevations in the vertical (Xue et al. 2006). Observations of Z, and particularly Z_{DR}, can be quite noisy and can lead to a noisy analysis (Putnam et al. 2019). The observations are smoothed in two passes by first using a five-point along-the-radial running average on the raw observations and then a square nine-point median filter after the observations have been interpolated to the model grid.

One of the critical components of radar DA involves assimilating clear-air observations that help suppress spurious convection in the model. However, because the KOUN observations are sector scans, there is a large portion of the domain where coverage from KOUN is not available. Clear-air observations from the nearby WSR-88D at KTLX, which have the same 250-m gate spacing as KOUN, are combined with each KOUN volume to help suppress spurious convection outside of the sector scans (NOAA/NCEI 1991; Tong and Xue 2005). Areas where convection is observed by KTLX outside of the KOUN sector scans are marked as missing.

c. Data assimilation settings

The observations are assimilated on the 1-km grid using the ensemble square-root filter (EnSRF; Whitaker and Hamill 2002) originally developed for the Advanced Regional Prediction System with polarimetric radar data assimilation capabilities (Xue et al. 2006; Jung et al. 2012; Zhu et al. 2020). The system also directly supports the WRF model and has an efficient parallelization implementation for high density observations (Wang et al. 2013). The prior ensemble spread is restored by a factor of 0.98 using the Whitaker and Hamill (2012) "relaxation to prior spread" covariance inflation method to help maintain ensemble spread. A covariance localization radius of 3 km in the horizontal and vertical is used to prevent spurious correlations away from the observations (Gaspari and Cohn 1999).

The Z and Z_{DR} observations are assimilated using operators that are based on T-matrix calculations and use lookup tables to precalculate a portion of the operator for computational efficiency (Putnam et al. 2019). Specifically, the Z_h and Z_v operators of Jung et al. [2010, their Eqs. (3) and (4)], which require computationally expensive numerical integration, are modified. A simplified example of the Z_h operator is given here:

$$Z_h = \frac{4\lambda^4}{\pi^4 |K_w|^2} \int |f_a(\pi)|^2 N_0 e^{-\Lambda D}\, dD, \tag{1}$$

where λ is the radar wavelength, K_w is the dielectric factor for water, $f_a(\pi)$ is the backscattering amplitude for the major axis of the hydrometeor, N_0 is the intercept parameter of the PSD, Λ is the slope of the PSD, and D is the hydrometeor (particle) diameter. The Z_h and Z_v operators were modified in Putnam et al. (2019) to precalculate Z_h and Z_v using a summation over a range of possible hydrometeor diameters with the values stored in tables based on the slope (Λ) parameter of the PSD for each hydrometeor category prior to assimilation. The N_0 can be taken out of the summation leaving each summation based on Λ, with an example for rain given here:

$$Z_h = \frac{4\lambda^4}{\pi^4 |K_w|^2} N_0 \sum_{i=0.0}^{8.0} |f_a(\pi)|^2 e^{-\Lambda D} \Delta D, \tag{2}$$

where the summation is performed for drop sizes (i) 0.0 to 8.0 mm [Eq. (2) from Putnam et al. (2019)]. The Λ value is calculated during assimilation based on the model predicted hydrometeor q and N_t and the corresponding closest value of Λ from the precalculated tables is used to determine Z_h and Z_v. Finally, Z_H (Z) and Z_V are determined by adding up contributions from Z_h and Z_v for all hydrometeor categories (x) present:

$$Z_H = 10 \log_{10}(Z_{h,x_1} + Z_{h,x_2} + \cdots), \tag{3}$$

$$Z_V = 10 \log_{10}(Z_{v,x_1} + Z_{v,x_2} + \cdots), \tag{4}$$

with Z_{DR} given by the ratio of these contributions from Z_h and Z_v:

$$Z_{DR} = 10 \log_{10}\left(\frac{Z_{h,x_1} + Z_{h,x_2} + \cdots}{Z_{v,x_1} + Z_{v,x_2} + \cdots}\right) \tag{5}$$

[adapted from Eqs. (14), (15), and (16) of Jung et al. (2008a)]. The graupel and hail categories in the NSSL scheme have variable density and a range of densities from 100 to 900 kg m^3 in 100 kg m^3 increments are included for those lookup tables in addition to Λ. This method better represents the range of possible dual-pol values while saving significant computational time that makes using the T-matrix based calculations practical.

The observation error standard deviations are assumed to be 6 dB for Z, 4 m s^{-1} for V_r, and 0.6 dB for Z_{DR} based on values determined in Putnam et al. (2019). The observation errors are assumed to be uncorrelated as required by the EnSRF algorithm used (Whitaker and Hamill 2002), thus the observation error covariances are assumed to be 0. Partly to account for potential error correlations, the observation errors used are higher than the typical measurement errors (Hilton et al. 2009; Fowler et al. 2018). The assumed errors also include those from the observation operator, representativeness, and sampling. Jung et al. (2008b) also found that the assumption the errors are uncorrelated was practical using the same base EnSRF code and observation operators for dual-pol assimilation as in this study. Clear-air Z observations are assimilated everywhere while V_r observations are assimilated in precipitation areas where $Z > 10$ dBZ. A threshold to assimilate Z_{DR} of $Z_{DR} >$ 3.0 dB is used at heights less than 3500 m and $Z_{DR} > 0.75$ dB at heights greater than 3500 m, or the approximate environmental melting layer. These thresholds are chosen to focus on assimilating the high values of Z_{DR} seen in the Z_{DR} arc signature below the melting layer and the Z_{DR} column above the melting layer where prior studies have shown that the Z_{DR} observations have a positive impact on the microphysical and dynamical state of the storms (Carlin et al. 2017; Putnam et al. 2019). Outside of these regions of significant values, smaller Z_{DR} observations can be quite noisy compared to Z (Jung et al. 2008b) and lead to a poor analysis of state variables when trying to fit them to Z_{DR} observations. This differs from a prior dual-pol DA study (Putnam et al. 2019) where observations were limited to below the melting layer and allows for observations from the Z_{DR} column to impact the analysis.

During each assimilation cycle, Z and V_r observations are assimilated first and then Z_{DR} observations are assimilated. Putnam et al. (2019) showed improved analyses with such a sequence because adjustments to the model state variables based on the Z_{DR} observations can be overwhelmed from more significant adjustments by Z observations due to the greater number and range in magnitude of Z observations. Additionally, the Z, V_r, and Z_{DR} observations are assimilated at every other grid point following Putnam et al. (2019); assimilating the data every grid point was found to sometimes overadjust the model state that can show up as poor combinations of hydrometeor mixing ratios (q) and number concentrations (N_t). The insufficient observational constraint and large uncertainty with the covariance estimation from the relatively small ensemble are believed to be the cause. The reduction in observation density also helps account for the potential of observation error correlations that are assumed to be 0 in our EnKF system (Dando et al. 2007). The conventional surface observations from the Oklahoma Mesonet are assimilated prior to the radar observations in the following order with errors of 1.5 m s^{-1} for u and v, 2 K for T, 2 K for T_d, and 2 hPa for p. The localization radius for these observations is 100 km horizontally and 6 km vertically.

4. Results

The results are presented in three sections. First, we assess the overall storm structure and evolution based on probabilistic forecasts of reflectivity. Second, differences in the predictions of storm hazard products are assessed, including updraft helicity and hail, which are an important feature of the WoF system (Stensrud et al. 2009). Finally, the evolution of model state features including the storm cold pool and updraft are compared to investigate how assimilating the additional Z_{DR} observations, specifically those associated with the Z_{DR} column, over multiple DA cycle windows contributes to differences in the subsequent ensemble forecasts.

a. Evaluation of ensemble forecasts

The forecast storm evolution is assessed by comparing observed Z with forecast probability-matched ensemble mean Z (PMEM; Ebert 2001). The evaluation is done in 30-min increments from 2300 UTC 31 May 2013 until 0100 UTC 1 June 2013 (5 forecast times) for the EXPZ and EXPZZDR forecasts initialized at 2230 UTC (Fig. 2), 2245 UTC (Fig. 3), and 2300 UTC (Fig. 4). The PMEM first ranks all Z values from all members in increasing order and all Z values from the ensemble mean in increasing order separately. The ranked Z values from the ensemble members are then moved to the location on the grid where the Z value of the same rank in the ensemble mean is located to account for location differences over small scales where Z values could significantly vary or be 0, which leads to a low bias in mean Z. The observed Z plotted is from KTLX, not KOUN, since the KTLX observations cover all observed storms and the KOUN sector scans miss storms to the north and west of the storm of interest. The observations at 2300 UTC include a mature supercell over El Reno as well as an additional storm to the north that eventually moves over Stillwater, Oklahoma, at 0000 UTC, with severe winds and hail reported in the vicinity (SPC 2019). In the discussion of the results, these storms will be referred to as the "El Reno" and "Stillwater" storms and are noted by the letters A and B, respectively, in Fig. 2d.

Both forecast experiments initialized at 2230 UTC produce forecasts of the El Reno storm that generally move at a slightly faster speed and are located in the same vicinity of the observed storm as it passes east over Oklahoma City (Fig. 2). Additional convection develops to the northwest of the storm, but the ensembles do not replicate the repeated initiation and training of thunderstorms over the Oklahoma City region seen in the observations and discussed in section 2. This convection in the forecasts is displaced farther north and weakens quickly as the storms move to the east after 0000 UTC (Figs. 2i,n,j,o). The forecasts of the El Reno storm overall are similar except for in EXPZ_2230 at 0100 UTC where stronger convection develops to the southwest of the storm and begins to move southeastward, beginning to surpass the progression of the

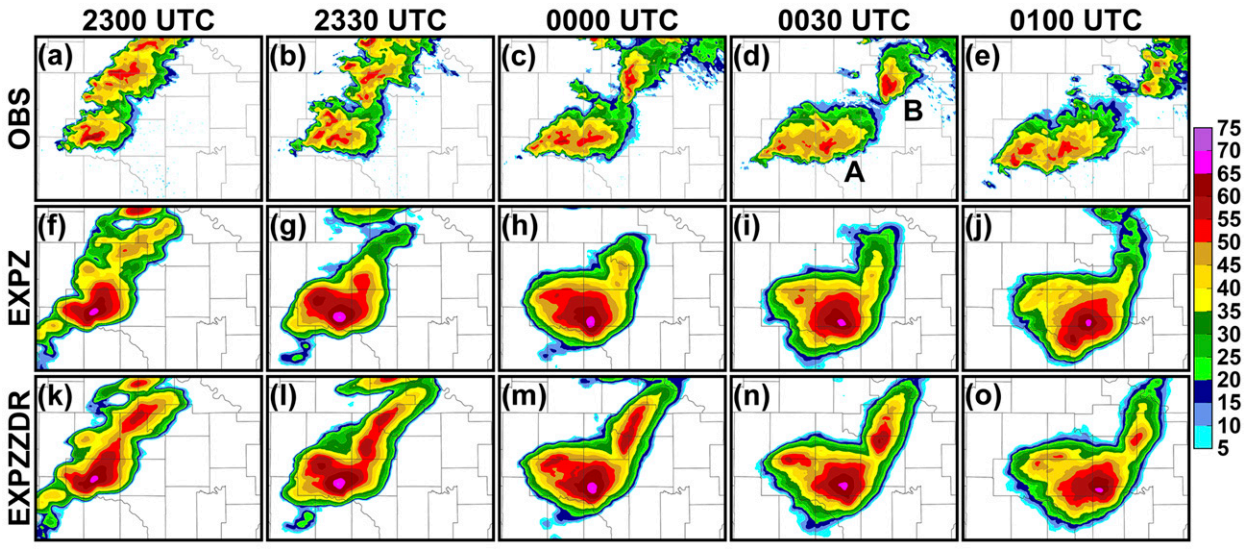

FIG. 2. Observed reflectivity (Z) from (a)–(e) 2300 UTC 31 May to 0100 UTC 1 Jun 2013 in 30-min increments as well as forecast probability-matched mean Z plotted at the first level above the surface from (f)–(j) EXPZ_2230 and (k)–(o) EXPZZDR_2230. The El Reno and Stillwater storms are noted by the letters "A" and "B" in (d), respectively.

observed El Reno storm to the south and east (Fig. 2j), which differs from EXPZZDR_2230 and the observations. The experiments differ more in the forecast of the northern Stillwater storm. The storm weakens rapidly by 0000 UTC in EXPZ_2230 (Fig. 2h), and the remaining convection at 0100 UTC is not identifiable as a separate storm from the El Reno supercell (Fig. 2j). In contrast, the convection is maintained for a longer period of time in EXPZZDR_2230, with a similar strength cell compared to the observations at 0100 UTC (Fig. 2o).

The storm development and propagation are more similar between the forecasts initialized at the later 2245 UTC and 2300 UTC initialization times (Figs. 3 and 4). In Figs. 3f–j, the core of the El Reno storm in EXPZ_2245 begins to weaken as it moves east during the forecast period. The reflectivity core peaks in intensity at 0000 UTC (Fig. 3h) and then decreases in intensity and loses its identity by 0100 UTC. In contrast, the similar reflectivity core in EXPZZDR_2245 UTC remains stronger and continues to move eastward between 0000 and 0100 UTC (Figs. 3m–o). The convection that develops to the west of the El Reno storm noted in Fig. 2 is more intense relative to the El Reno storm and actually surpasses the El Reno storm in intensity by 0030 UTC in EXPZ_2245 (Fig. 3i). This convection moves southeastward in a similar manner to that seen in EXPZ_2230 UTC. Both forecasts show this pattern in

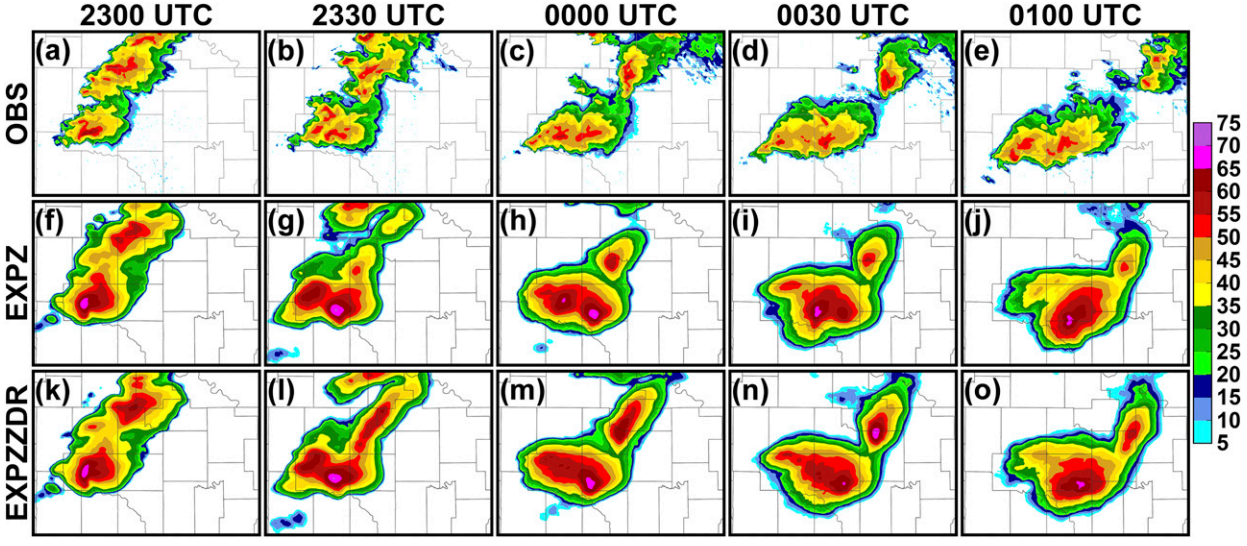

FIG. 3. As in Fig. 2, but for EXPZ_2245 and EXPZZDR_2245.

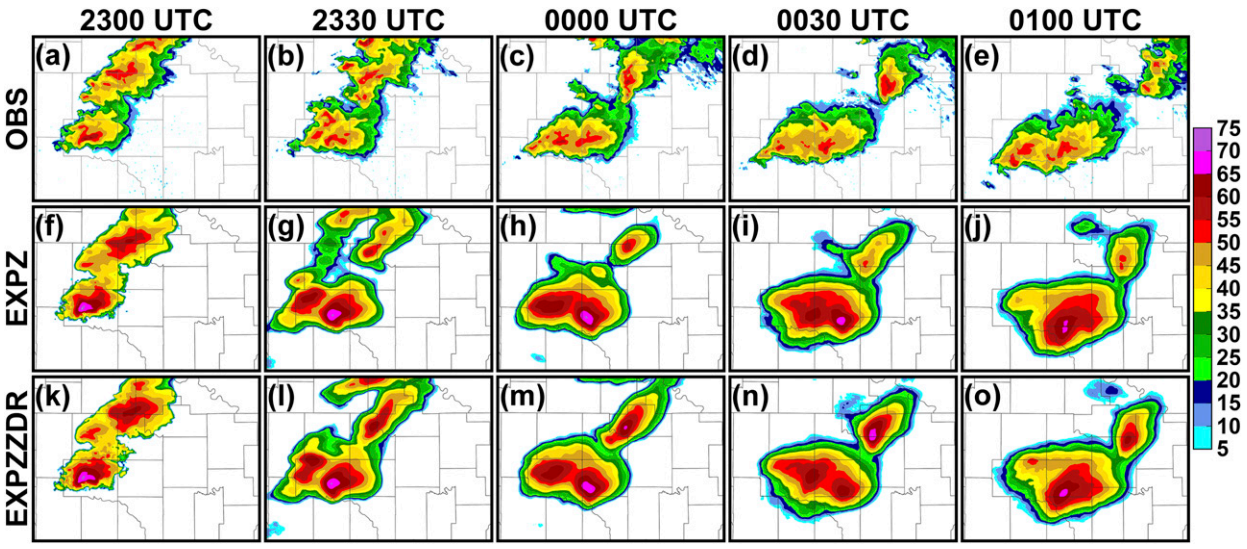

FIG. 4. As in Fig. 2, but for EXPZ_2300 and EXPZZDR_2300.

EXPZ_2300 and EXPZZDR_2300 (Fig. 4). The El Reno storm weakens while the storm that develops to the west becomes more dominant as it moves to the southeast, in a manner more typical of outflow-dominant convection, in contrast to the observations, where the El Reno storm remains intense and continues to move east at 0100 UTC (Figs. 4e,j,o). It should be noted that there is a tendency for the NSSL scheme to produce higher Z values in the background forecasts and subsequently the EnKF analyses (Figs. 4f,k), due to the scheme's tendency to predict large hail as well as excessive size sorting, and the tendency for the EnKF to overestimate larger rain drops when independently estimating the q and N_t state variables (Dawson et al. 2013; Johnson et al. 2016, 2019). Due to the tendency for the NSSL scheme to produce too high Z values, we focus our qualitative analysis and interpretation of the forecast PMEM Z from the two experiments in terms of relative differences between the two experiments compared to the relative differences in the observations over time.

The EXPZZDR experiment forecasts that are initialized after longer DA periods, EXPZZDR_2245 and especially EXPZZDR_2300, exhibit more similar characteristics to the EXPZ experiments for the El Reno storm. In contrast to the evolution of the El Reno storm at later initialization times, the results for the Stillwater storm in the EXPZZDR experiments continue to improve compared to the EXPZ experiments, as the DA window covers more of the development of the storm. The Stillwater storm continues to weaken after 0000 UTC in EXPZ_2245 and EXPZ_2300 (Figs. 3h–j and 4h–j), while the storm in EXPZZDR_2300 increases in intensity between 0000 and 0030 UTC before decreasing in intensity (Figs. 4m–o) in a similar manner to the observations by 0100 UTC (Figs. 4c–e).

The similarities and differences of the location and coverage of convection for the El Reno and Stillwater storms are even more obvious when comparing probabilistic forecasts of Z. Figure 5 contains the 5-km neighborhood ensemble probability of Z greater than 15 dBZ at 0000, 0030, and 0100 UTC, with the threshold of 15 dBZ chosen to assess the overall predicted coverage of precipitation. The differences in the forecasts at all three forecast initialization times are directly compared in Fig. 5 in contrast to evaluating the evolution of each of the forecasts in Figs. 2–4. The precipitation coverage is similar between the two experiments at all times for the El Reno storm. Both experiments capture the placement of the eastern portion of the convection and have noticeable but very low probabilities for the training storms following the El Reno storm to the west. The complex development of these training storms is a possible area for future study. The plots also highlight the improvement in the prediction of the Stillwater storm in the EXPZZDR experiments. At all three forecast times there are higher probabilities compared to the EXPZ experiments, and these probabilities increase with forecasts initialized after more DA cycles that cover the early development of the storm (Figs. 5k,l).

The forecast initialization times from the EXPZZDR experiments and EXPZ experiments that produce improved forecasts of the El Reno and Stillwater storms are not the same. The EXPZZDR forecasts better predict the El Reno storm after only a few DA cycles early in the period (EXPZZDR_2230) while the EXPZZDR experiments better predict the Stillwater storm at the later forecast initialization times (EXPZZDR _2300). These results may appear conflicting. However, the El Reno storm is less sensitive to when the EXPZZDR forecasts are initialized during the assimilation period because the storm organized more rapidly early in the period, before the later forecasts are initialized, while the Stillwater storm evolved from a cluster of storms later in the period, across the forecast initialization times (Fig. 5). The later forecasts of the Stillwater storm increasingly include more DA cycles that cover the storm organization. Overall, EXPZZDR forecasts initialized after DA windows that assimilate Z_{DR} for several cycles covering the earlier stages of storm development and organization produce the most improved forecasts compared to

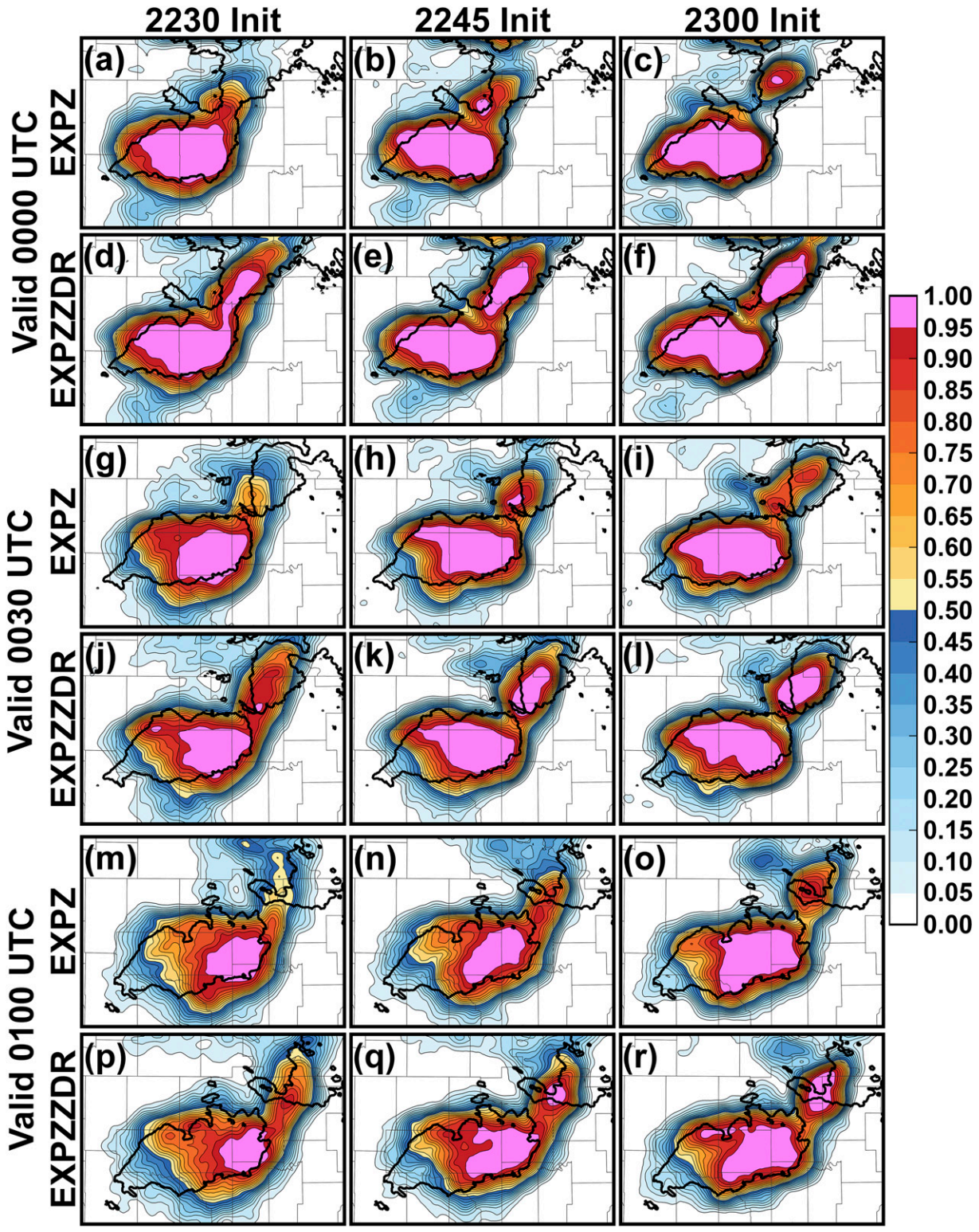

FIG. 5. Probability of reflectivity (Z) greater than 15 dBZ for EXPZ valid at 0000 UTC 1 Jun 2013 from the forecasts initialized at (a) 2230, (b) 2245, and (c) 2300 UTC 31 May 2013 and for (d)–(f) EXPZZDR as well as the same probabilities for Z valid at 0030 UTC 1 Jun 2013 for (g)–(i) EXPZ and (j)–(l) EXPZZDR and at 0100 UTC 1 Jun 2013 for (m)–(o) EXPZ and (p)–(r) EXPZZDR. Observed Z greater than 15 dBZ is outlined in black.

the EXPZ forecasts. The results also indicate there may be less need for the help of Z_{DR} data in addition to Z and V_r data for mature storms.

We examined the root-mean-square innovations (RMSIs) and the ensemble spreads in terms of Z and Z_{DR} for all the initial conditions. The Z values are calculated in areas where the predicted or observed Z is greater than 15 dBZ and the Z_{DR} values are calculated where observed Z_{DR} is greater than 3.0 dB below 3500 m or 0.75 dB above 3500 m, the thresholds for Z_{DR} assimilation. We found that the RMSIs and spreads do not differ much between experiments EXPZ and EXPZZDR for either Z or Z_{DR}. The RMSIs for Z and Z_{DR} are ~7–9 dB, and ~2 dB, respectively, while the corresponding spreads are ~6–8 dB and ~0.5 dB, respectively. Within EnKF radar DA, and EnKF DA in general, underdispersion in terms of spread is a common problem (Dowell and Wicker 2009; Aksoy et al. 2009; Jung et al. 2012; Yussouf et al. 2013; Houtekamer et al. 2014; Putnam et al. 2014; Romine et al. 2014; Wheatley et al. 2014; Snook et al. 2015; Houtekamer and Zhang 2016; Carrió et al. 2019), and here we see more underdispersion in Z_{DR} while the spreads of Z are actually relatively large. The latter should be related to the fact that our calculations do not include points where observed or predicted Z is below 15 dBZ. Given that within EnKF DA cycles the ensemble spread is somewhat artificially tuned through covariance inflation, forecast quality is often a better indication of the initial condition quality than the analysis spread.

One of the additional benefits of using an ensemble forecast is that the differences between each member provide a characterization of the forecast skill and uncertainty (Ehrendorfer 1997; Sivillo et al. 1997; Toth et al. 2001; Satterfield and Szunyogh 2010; Yokohata et al. 2012; Loeser et al. 2017), including in studies that focused on convective-scale forecasts (Clark et al. 2011; Evans et al. 2014; Snook et al. 2015; Iyer et al. 2016; Loken et al. 2017; Putnam et al. 2017; Erickson et al. 2019). To assess the performance of the ensemble experiments, we look at both the area under the relative operating characteristic (ROC) curve (AUC) and forecast reliability. The AUC is a forecast skill score that considers the probability of a hit versus the probability of a false alarm between the ensemble forecasts and the observations (Mason 1982; Mason and Graham 1999). The AUC is calculated for Z values from the simulated forecast results and observations from the 0.5° tilt of KTLX from 10 to 50 dBZ using a 5-km neighborhood (Fig. 6). The score is calculated for all experiments for the El Reno and Stillwater storms over the domain and 0000–0100 UTC time frame considered in Figs. 2–5. A 95% confidence interval is provided by recalculating the AUC 1000 times using a bootstrap sampling method. The bootstrapping is performed by taking a random sample of 36 members from the ensemble and recalculating the score based on that 36-member sample, with the range of those scores providing the confidence interval. The results show that not only are forecasts from both experiments skillful over the range of Z values considered, but that the forecasts of EXPZZDR have higher skill than the EXPZ results for almost all Z values at all forecast times. More improvement is seen for EXPZZDR_2230 and EXPZZDR_2245 (Figs. 6a,b,d,e,g,h), which both showed improved forecasts of the El Reno and Stillwater storms compared to EXPZ_2230 and EXPZ_2245. The EXPZZDR_2245 forecast at 0030 UTC (Fig. 6e) shows the most improvement in skill for the higher Z values 45–50 dBZ, which corresponds with the development of the intense convection west of the El Reno storm in the EXPZ_2245 forecast noted in Fig. 3i. The least improvement is seen in EXPZZDR_2300 compared to EXPZ_2300, which showed similar forecasts of the El Reno storm, with new convection to the west surpassing the El Reno storm in intensity by 0100 UTC (Fig. 6i).

The forecast reliability diagram provides a quantitative assessment of the amount of certainty for an ensemble forecast by comparing the range of forecast probabilities of an outcome, in this case the probability of $Z > 15$ dBZ, to the frequency that values of $Z > 15$ dBZ are observed (Fig. 7; Brown 2001; Hudson 2017). The calculation uses the same 5-km neighborhood for the same 0.5° tilt of KTLX and timeframe as in Fig. 6. The 15-dBZ threshold is chosen to evaluate the coverage of precipitation considered in Fig. 5. Areas above the included black dashed diagonal line indicate when the probabilities are underforecast, while areas below the line indicate when the probabilities are overforecast (overconfident), and blue shading indicates when the forecast probabilities are skillful. In general, all forecasts for both experiments are skillful for most probabilities of $Z > 15$ dBZ at most forecast times. In particular, EXPZDR_2230 is more reliable than EXPZ_2230 at 0000 UTC when EXPZ_2230 significantly overforecasts $Z > 15$ dBZ (Fig. 7a). This corresponds with the improved forecasts of both the El Reno and Stillwater storms at this time. As with the AUC, the forecasts are more similar at the later forecast initialization time (2300 UTC), when the prediction of the El Reno storm is more similar between the two experiments (Figs. 7f,i). The EXPZ experiments are more reliable for some probabilities at some forecast times, specifically when EXPZZDR_2300 overforecasts higher probabilities of $Z > 15$ dBZ at 0000 UTC (Fig. 7c). However, in general, the EXPZZDR experiments are at least similar if not more reliable than the EXPZ experiments overall. Along with the AUC, these ensemble forecast verification metrics show that the EXPZZDR experiments perform at least as well as, and in many cases improve upon, the EXPZ experiments, indicating that conclusions drawn from the qualitative evaluation of the results are reasonable. The results also further demonstrate how the assimilation of Z_{DR} over a smaller timeframe covering the earlier stages of storm development provide a more skillful and certain ensemble forecast of the storms, specifically the larger improvements seen in EXPZZDR_2230 over EXPZ_2230.

b. *Evaluation of derived forecast products and predicted hazards*

The goal of the WoF system is to generate a continuous flow of rapidly updating probabilistic model guidance of severe convective hazards once the thunderstorm initiates (Stensrud et al. 2009). In this section, we evaluate mesocyclone and hail forecast products to determine if assimilating Z_{DR} over various DA windows not only improves the forecast coverage and intensity of storms but their associated severity of hazards as

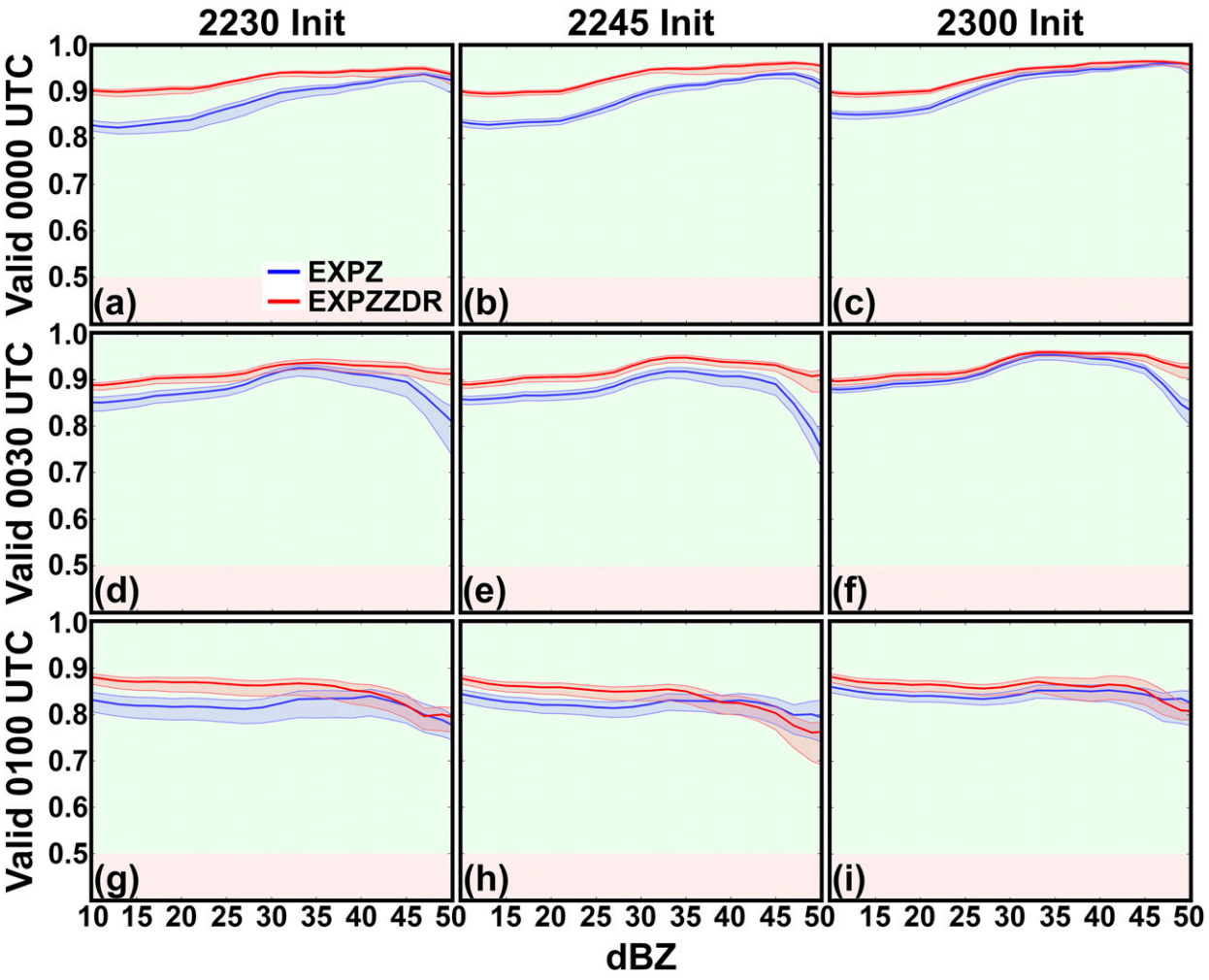

FIG. 6. AUC skill score calculated for Z values from 10 to 50 dBZ for EXPZ (blue) and EXPZZDR (red) valid at 0000 UTC 1 Jun 2013 for the forecasts initialized at (a) 2230, (b) 2245, and (c) 2300 UTC 31 May 2013, as well as for (d)–(f) 0030 and (g)–(i) 0100 UTC. A 95% confidence interval is provided within the corresponding blue and red shading. The background green shading indicates a skillful forecast and the pink shading indicates no forecast skill.

well. First, probabilistic forecasts of updraft helicity (UH) are considered. UH is the product of vertical vorticity and updraft velocity integrated over a given depth (Kain et al. 2008) and serves as a proxy for mesocyclone strength as well as the associated increased potential for hail and tornadoes in ensemble forecasts (Sobash et al. 2011; Clark et al. 2012, 2013; Yussouf et al. 2015; Gallo et al. 2016; Sobash et al. 2016). Figure 8 contains swaths of the grid-based probability of midlevel UH (2–5-km) associated with the midlevel mesocyclone exceeding 50 $m^2 s^{-2}$ calculated every 5 min between 2300 UTC 31 May and 0100 UTC 1 June 2013. Contours of the NSSL's Multi-Radar Multi-Sensor (MRMS) azimuthal shear product (NOAA/NSSL 2014; Smith et al. 2016) calculated using observed V_r (Smith et al. 2004) are overlaid to mark the location of rotation in the observed storms.

EXPZZDR_2230 (Fig. 8d) predicts a UH swath that better follows the observed azimuthal shear associated with the El Reno storm compared to the swath in EXPZ_2230, which veers too far south and east (Fig. 8a). This increasingly southeasterly movement appears to follow the track of the new convection to the west of the El Reno storm seen in Fig. 2j, suggesting the predicted UH in EXPZ_2230 is no longer associated with the El Reno storm but rather with the subsequent new convection. The forecasts become more similar at the latter two initialization times (Figs. 8b–f), and both experiments predict UH tracks that are oriented more to the south and east of the observed azimuthal shear. This deviant UH track more closely follows the path of the storm that initiates later to the west of the El Reno storm and eventually supersedes the El Reno storm. UH probabilities are lower for the northern, Stillwater storm in all experiments overall, but EXPZZDR predicts increasingly higher probabilities than EXPZ with later forecast initialization times (Figs. 8d–f). The tracks are displaced to the south of the observed azimuth shear but forecast and observed track lengths are approximately the same.

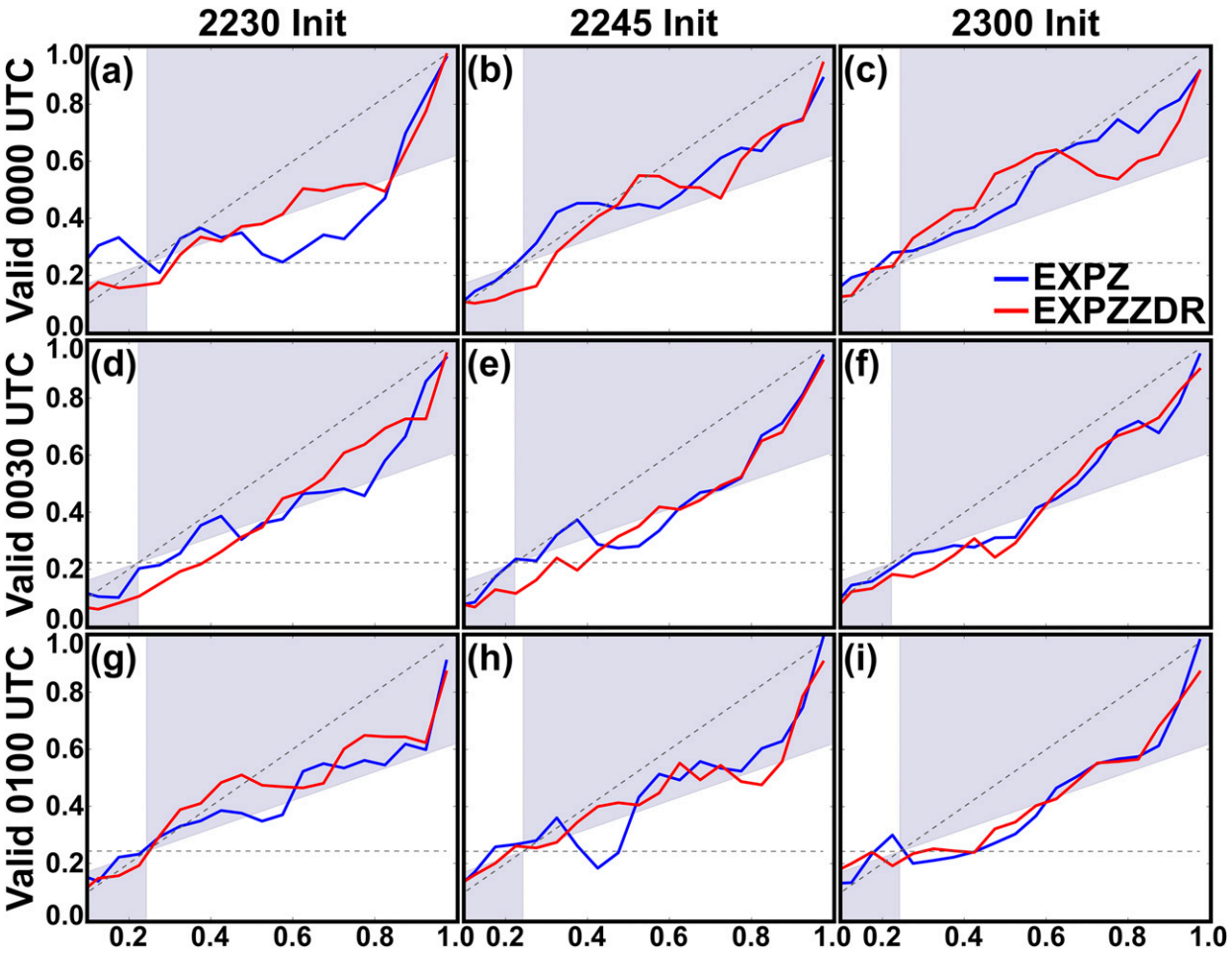

FIG. 7. Reliability diagrams for EXPZ (blue) and EXPZZDR (red) for the probability of $Z > 15$ dBZ valid at 0000 UTC 1 Jun 2013 for the forecasts initialized at (a) 2230, (b) 2245, and (c) 2300 UTC 31 May 2013, as well as for (d)–(f) 0030 and (g)–(i) 0100 UTC. The black dashed diagonal line indicates perfect reliability, and the black dashed horizontal line indicates a forecast of climatology. The blue shading indicates a skillful forecast.

Swaths of hail probabilities are shown in Fig. 9. The probability of hail exceeding 5 mm in diameter at the surface is calculated every 5 min from the model output over the same forecast window as UH (2300 to 0100 UTC). Maximum hail diameters are determined following the method first employed by Snook et al. (2016), which diagnoses the largest observable hailstone from hail PSDs at each grid point, using the Thompson hail method (Thompson et al. 2018) for the NSSL microphysics scheme in a similar manner to Labriola et al. (2019b). Also following Snook et al. (2016), radar indicated regions of hail identified by the Park et al. (2009) hydrometeor classification algorithm (HCA) using KTLX data (NOAA/NCEI 1991) are overlaid on the plots. Probabilistic hail size forecasts for the El Reno storm are very similar in amplitude and coverage for all forecast initialization times. However, there is an increase in forecast probabilities between the two sets of experiments for the Stillwater storm. Both EXPZZDR_2245 (Fig. 9e) and EXPZZDR_2300 (Fig. 9f) predict swaths of higher hail probabilities than their EXPZ counterparts (Figs. 9b,c). EXPZZDR_2300 in particular better predicts the probability of 5 mm hail exceeding 90% within the observed hail path. The Stillwater storm is weaker and smaller compared to the El Reno storm but still produces severe hail, and the EXPZZDR forecasts highlight this hail threat better.

c. *Evaluation of the analyzed state*

The evaluation of the storm evolutions and predicted hazards in sections 4a and 4b indicates that there is an improvement in forecasts of storms when Z_{DR} is assimilated in the EXPZZDR experiments, and the impact is greater when the DA window covers more of the storm development. Previous observational studies of Z_{DR} have indicated that there is a sharp increase in the values of Z_{DR} associated with the updraft, the Z_{DR} column, as the storm initiates (Kumjian and Ryzhkov 2008). Carlin et al. (2017) also showed improved forecasts of UH when Z_{DR} columns are used to identify updrafts during cloud analysis DA. To investigate how assimilation of Z_{DR} affects the strength of the updrafts, we compare the analyzed

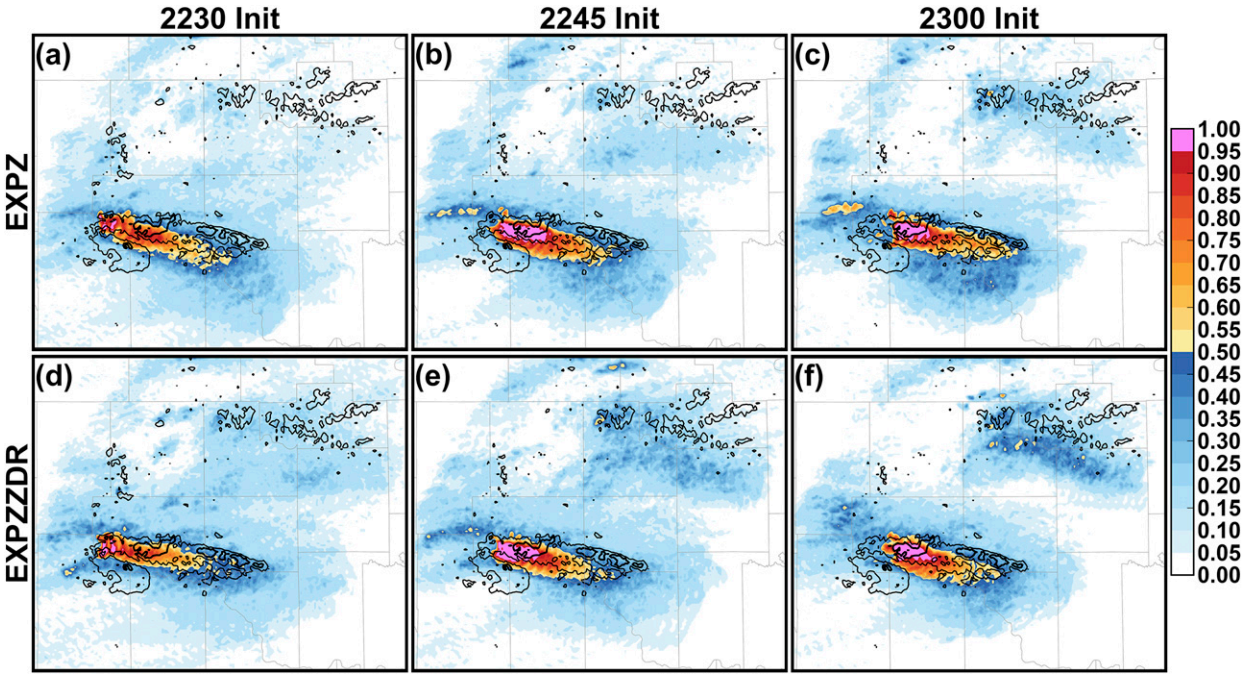

FIG. 8. Swaths of the probability of midlevel UH (2–5 km) greater than 50 $m^2 s^{-2}$ from 2300 UTC 31 May to 0100 UTC 1 Jun 2013 for EXPZ forecasts initialized at (a) 2230, (b) 2245, and (c) 2300 UTC 31 May 2013 as well as for (d)–(f) EXPZZDR. Contours of observed azimuthal shear of 0.006 and 0.012 s^{-1} are outlined in black.

vertical velocity (w) at the height of the average melting layer of the domain, where supercooled raindrops breach the melting layer, as well as the maximum w for the earliest (2230 UTC) and latest (2300 UTC) forecast initialization times (Fig. 10). The w values are larger and more focused for the El Reno storm in EXPZZDR_2230 than in EXPZ_2230 both at the melting layer and for the vertical maximum. The vertical maximum w in particular shows a larger, circular region of w values exceeding 50 m s^{-1}. However, the values are very similar for the 2300 UTC experiments. Sections 4a and 4b showed that the EXPZZDR forecasts more closely resembled the EXPZ forecasts and deviated more from the observations at the later forecast initialization times when the El Reno storm was more mature. For the Stillwater storm, the EXPZZDR_2300 analysis, which includes more DA cycles that cover the development of the storm, shows larger w values than the EXPZ_2300 analysis. The later initialized EXPZZDR_2300 forecast showed more improvement in sections 4a and 4b over EXPZZ_2300 compared to the differences between EXPZZDR_2230 and EXPZ_2230. The assimilation of the Z_{DR} observations during DA windows that adequately cover initial storm organization show an increase in the strength of the updraft, and the forecasts initialized with this stronger updraft show improvement compared to the observations over those experiments that did not assimilate Z_{DR}.

Another difference between the two sets of experiments is the prediction of the northern, Stillwater storm across all EXPZZDR forecasts compared to the EXPZ forecasts, where the storm barely forms or weaken quicker depending on the forecast initialization time. The evolution of the El Reno storm and subsequent convection is also improved in EXPZZDR_2230 compared to EXPZ_2230, where new convection to the southwest begins to overtake the El Reno storm. The analyzed surface temperature (T) and dewpoint temperature (T_d) fields used to initiate the forecasts at 2230 UTC and 2300 UTC are compared in Fig. 11 (2230 UTC) and Fig. 12 (2300 UTC) [Oklahoma Mesonet observations are overlaid on all plots (Oklahoma Climatological Survey/Oklahoma Mesonet 1994)]. EXPZ analyzed T is cooler in the storm cold pools than EXPZZDR. The differences are most pronounced at 2300 UTC, with the coldest surface temperatures overall associated with the EXPZ_2300 Stillwater storm cold pool. EXPZ analyzed T_d is also lower than EXPZZDR, and the driest air is again seen in the EXPZ_2300 Stillwater storm cold pool.

While a cold pool is an important component to an organized supercell (Dawson et al. 2010), a cooler, drier cold pool may lead to a decrease in storm intensity as warm, moist air is cut off from and unable to maintain a mature and intense storm updraft. In fact, past studies have pointed out that cycled radar DA tends to overpredict the intensity of the cold pool (Dowell et al. 2011; Yussouf et al. 2013; Stratman et al. 2020). Cooler, drier cold pools are largely the result of the evaporation of smaller drops in rain drop size distributions (DSDs) that cool the air in storm downdrafts. Figure 13 contains a plot of the rainwater mean mass diameter (D_{nr}) for the 2230 and 2300 UTC analyses of EXPZ and EXPZZDR at an approximate height of 2200 m. This is roughly the level of free convection of the storm environment as indicated by the 0000 UTC 1 June 2013 Norman, Oklahoma, sounding. This height illustrates the distribution of rain DSDs in the vicinity of the storm

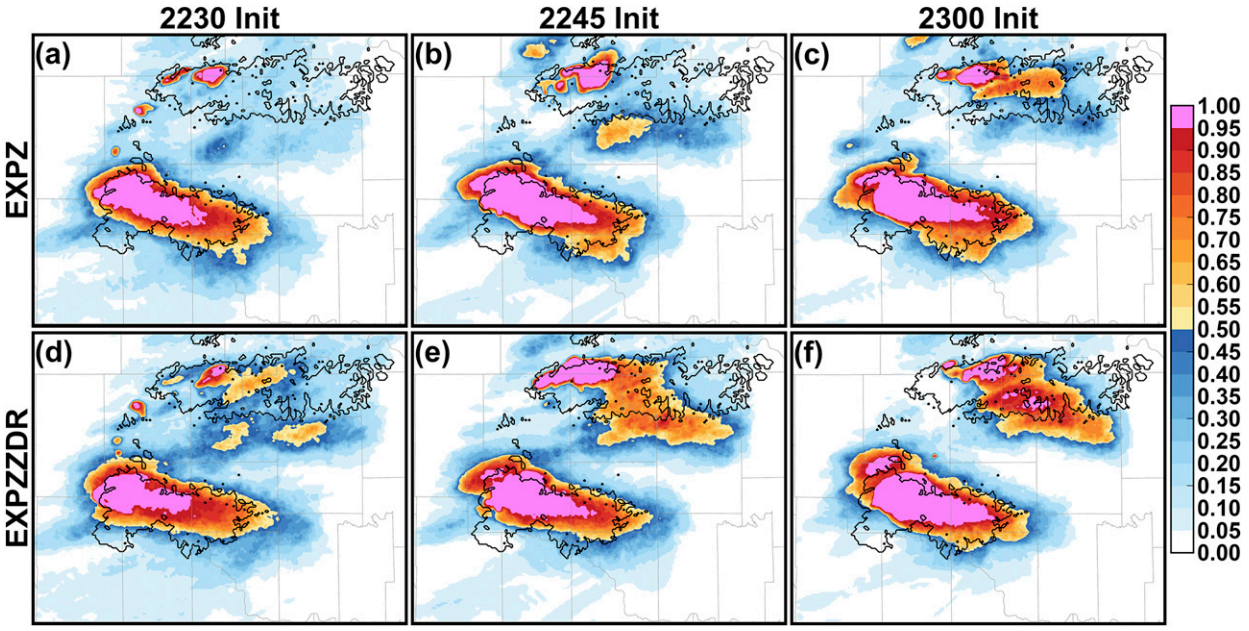

FIG. 9. Swaths of the probability of forecast surface hail max diameter greater than 5 mm from 2300 UTC 31 May to 0100 UTC 1 Jun 2013 for EXPZ forecasts initialized at (a) 2230, (b) 2245, and (c) 2300 UTC 31 May 2013 as well as for (d)–(f) EXPZZDR. Areas where radar observations are classified as hail using the Park et al. (2009) HCA are outlined in black.

cloud base before rain begins to fall below a stout capping inversion and evaporate. Figure 14 contains percentile-based histograms of D_{nr} values for both the El Reno and Stillwater storms at both analysis times for the model grid points associated with these storms (indicated by the black boxes in Fig. 13). The total number and range of D_{nr} values are found for each experiment and then distributed based on even 10% intervals to normalize the distributions in comparison to one another and reduce skewness due to outliers.

The D_{nr} values for the El Reno storm are similar between EXPZ_2230 and EXPZZDR_2230 for the main core of the storm. However, larger D_{nr} values extend farther east in the forward flank for EXPZZDR_2230. More importantly, there is an area of larger drops of about 1 mm in size associated with the rear flank on the southwest side of the storm (indicated by "1" in Figs. 13a,b). There are also higher values of D_{nr} associated with the core of the Stillwater storm in EXPZZDR_2230 compared to EXPZ_2230. The histograms in Figs. 14a and 14c show a shift toward higher values of D_{nr} for the Stillwater storm in EXPZZDR_2230 while there is no shift and only a higher number midrange D_{nr} values for the El Reno storm, likely from the widespread coverage of drops around 0.5 mm in

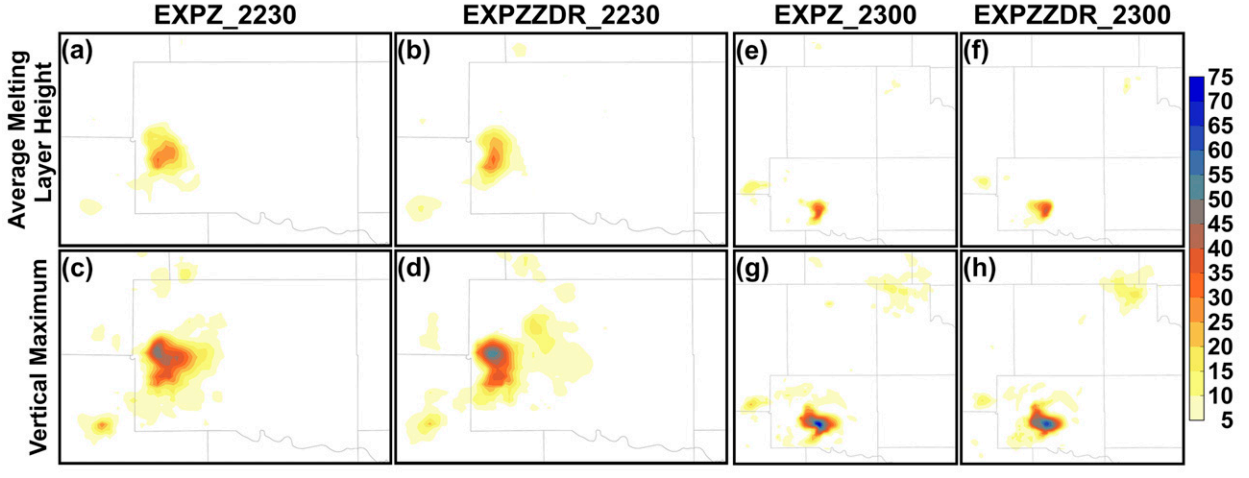

FIG. 10. Analyzed vertical velocity (w, m s^{-1}) at the average melting-layer height for (a) EXPZ_2230 and (b) EXPZZDR_2230 and the maximum w in (c) EXPZ_2230 and (d) EXPZZDR_2230 as well as the (e),(f) average melting-layer height w and (g),(h) maximum w for the EXPZ_2300 and EXPZZDR_2300 analyses.

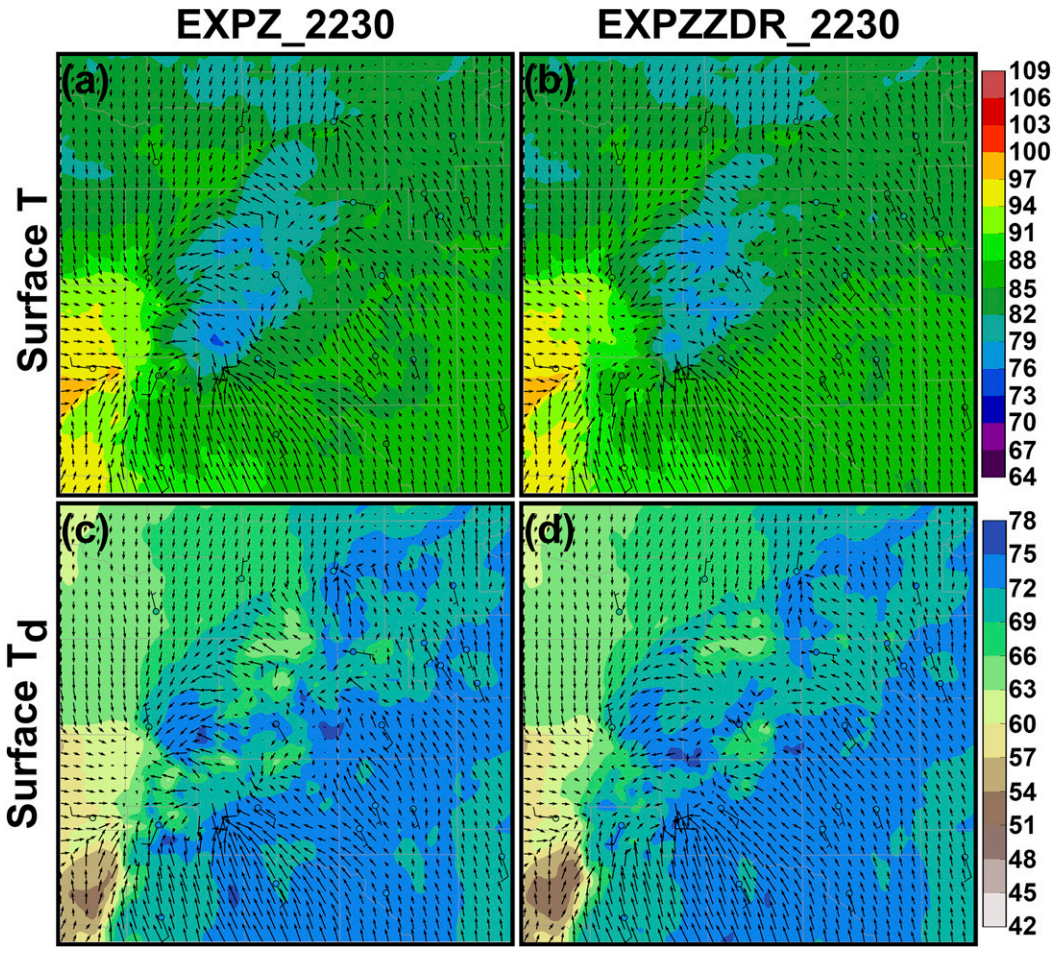

FIG. 11. Analyzed surface temperature (T, °F) at 2230 UTC 31 May 2013 for (a) EXPZ_2230 and (b) EXPZZDR_2230 and (c),(d) surface dewpoint (T_d, °F) for the same analyses. Strengthening analyzed surface winds are indicated by longer arrows. Observed surface temperature and wind barbs (mi h^{-1}; 1 mi $h^{-1} \approx 0.45$ m s^{-1}) from the Oklahoma Mesonet are included in the overlaid circles.

the forward flank. The differences in the D_{nr} values at 2230 UTC are subtle but still show increased D_{nr} in an organized rear flank for the El Reno storm and an increase in higher values in the core of the developing Stillwater storm, similar to the slightly warmer temperatures and more moist dewpoints in their cold pools at this time.

For the 2300 UTC analyses, larger D_{nr} values for the El Reno storm in EXPZZDR_2300 are more widespread and follow a more organized pattern with an improved "hook echo" structure similar to understood Z patterns on the rear side of the storm (indicted by "2" in Figs. 13c,d) and extend farther east and southeast within the forward flank (indicated by "3" in Figs. 13c,d). Larger values of D_{nr} extend much farther east in the forward flank for the Stillwater storm as well. Both histograms in Figs. 14b and 14d show a clear shift toward a higher number of larger D_{nr} values in the associated distributions based on assimilating the Z_{DR} observations above the two threshold values used. Overall, the storms in the EXPZZDR experiments have more widespread, dynamically organized distributions of larger drops compared to the EXP experiments around the storm base where high Z_{DR} observations are assimilated. This distribution of larger drops appears to result in less evaporation, where the distributions have been altered, as these drops fall to the surface. These results imply that the assimilation of Z_{DR} modifies the microphysical state of the analyzed storms in the EXPZZDR experiments by shifting the rain DSDs from the background forecast toward having more larger drops when they are expected based on the Z_{DR} observations (Fig. 14). The DSDs near Z_{DR} observations assimilated are altered to include a higher number of large drops and fewer small drops in a combination that provides a similar simulated Z value based on the total precipitation as the EXPZ experiments, similar to Putnam et al. (2019; e.g., Figs. 4f,k). The EXPZ forecasts initialized from these analyses have DSDs with smaller drops that result in stronger, drier cold pools and lead to storms dissipating more quickly than the observed storms (section 4a). It should be noted, however, that due to the thresholds used on the Z_{DR} observations assimilated, any

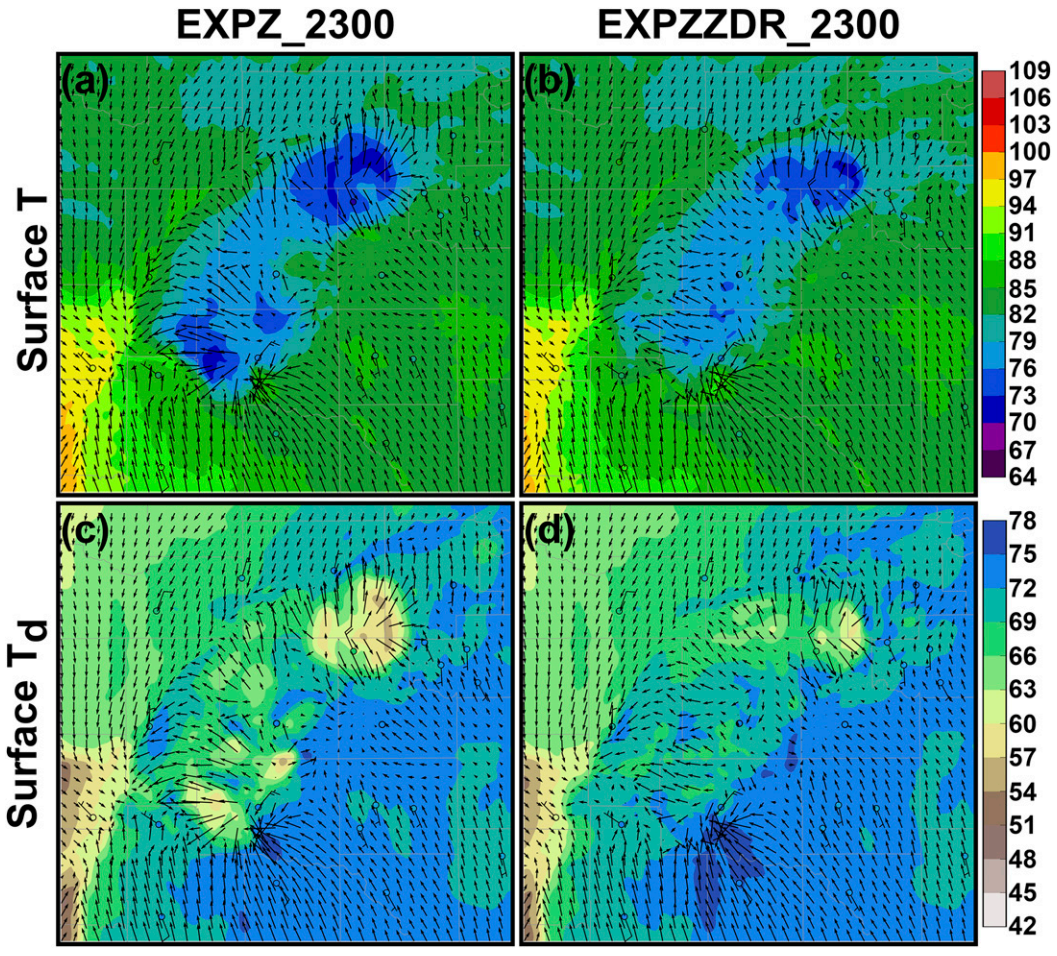

FIG. 12. As in Fig. 11, but for analyses at 2300 UTC for (a),(c) EXPZ_2300 and (b),(d) EXPZZDR_2300.

high bias present in the background forecast compared to the observations where Z_{DR} values are not assimilated will not be corrected. While there is a shift toward larger D_{nr} values seen in these results, the shift must be considered in the context that it only applies to areas where Z_{DR} observations are assimilated and thus is relative to any overall high bias in the background forecast that exists where the observations are not assimilated.

5. Summary

In this study, sector-scan dual-pol differential reflectivity (Z_{DR}) observations are assimilated in a storm-scale numerical model using an EnKF for the 31 May 2013 Oklahoma storm event. Attention is paid to two storms in central/northern Oklahoma: the El Reno storm that produced an EF3 tornado with significant hail and flooding over Oklahoma City and another storm to the north that produced severe wind and hail in the vicinity of Stillwater, Oklahoma. The dual-pol radar variables used in this study are collected by the National Severe Storm Laboratory's experimental WSR-88D radar (KOUN) that was run in an experimental sector-scan mode. The KOUN observations are used as a proxy for future dual-pol PAR, which is being developed as the future replacement for the aging WSR-88D network, to provide us the opportunity to experiment with the assimilation of sector-scan dual-pol observations in a WoF type system (Stensrud et al. 2009, 2013). Two sets of experiments initialize ensemble forecasts after increasing numbers of 5-min DA cycles to assess the impact of Z_{DR} assimilation on subsequent forecasts. The goal is to evaluate any improvements in forecasts from assimilating the additional sector-scan Z_{DR} observations and how this impact changes using DA windows of differing length, which future rapid-scan (~2-min) dual-pol PAR observations can take advantage of.

The two sets of experiments assimilate Z and V_r (EXPZ) or Z_{DR} in addition to Z and V_r (EXPZZDR). Assimilation starts at 2200 UTC 31 May 2013 and ensemble forecasts are initialized at 2230 UTC (30 min of DA), 2245 UTC (45 min of DA), and 2300 UTC (1 h of DA) to produce six total experiments identified by EXPZ or EXPZZDR and forecast initialization time (e.g., EXPZ_2230). The forecast probability-matched ensemble mean Z and probabilities of Z greater than 15 dBZ assess the evolution and precipitation coverage of the forecast storms. The El Reno storm in EXPZZDR_2230 better follows

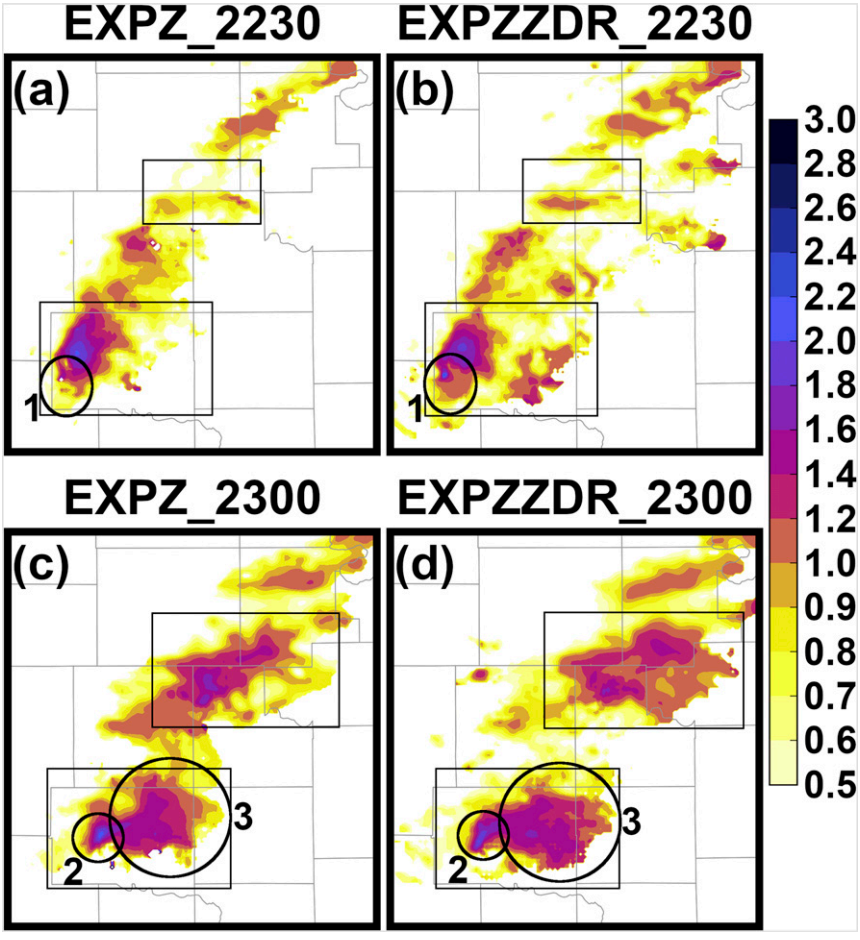

FIG. 13. Rain mean mass diameter (D_{nr}, mm) at the height of the environmental level of free convection (LFC) at 2230 UTC 31 May 2013 for the (a) EXPZ_2230 and (b) EXPZZDR_2230 analyses and at 2300 UTC 31 May 2013 for the (c) EXPZ_2300 and (d) EXPZZDR_2300 analyses. Black circles and numbers indicate areas of interest discussed in the text. The black boxes are the domains used for the histograms in Fig. 14.

the evolution and track of the observed storm than EXPZ_2230. However, the differences in the evolution of the El Reno storm between the EXPZ and EXPZZDR experiments decreases with later forecast initialization times because both experiments predict a secondary storm to the west that is too strong and supersedes the El Reno storm. Probabilistic forecasts of Z also show that the change in precipitation coverage between the experiments at different forecast initialization times is subtle for the El Reno storm, which organizes more rapidly during the first part of the assimilation period and is more mature during the latter half when the forecasts are initialized. On the other hand, the EXPZZDR experiment forecasts show continued improvement predicting the Stillwater storm for forecasts that are initialized later after more DA cycles that capture more of the storm organization. Updraft helicity and hail size probabilistic forecasts are also evaluated and show similar results. There is a noted improvement in the eastward orientation of the EXPZZDR_2230 track for the El Reno storm compared to the EXPZ_2230 track. EXPZZDR forecasts also predict increasingly higher UH and hail size probabilities than the EXPZ forecasts for later forecast times for the Stillwater storm.

An evaluation of the analyses provides insight into why the EXPZZDR experiments produced improved forecasts over the EXPZ experiments. The analyzed updraft speed is higher in EXPZZDR_2230 for the El Reno storm compared to EXPZ_2230, but both experiments at 2300 UTC produce similar results. Conversely, the analyzed updraft speed for the Stillwater storm is higher in EXPZZDR_2300 compared to EXPZ_2300. DA cycles assimilating larger Z_{DR} values from the Z_{DR} column covering the initial storm organization period appears to provide an improved analyzed updraft intensity and subsequent forecasts. Additionally, there is a shift toward larger analyzed rainwater mean mass diameter (D_{nr}) values at the storm base in the EXPZZDR experiments compared to the EXPZ experiments. The smaller D_{nr} values are more likely to increase evaporation and result in stronger cold pools that lead to faster storm dissipation in the EXPZ experiment forecasts.

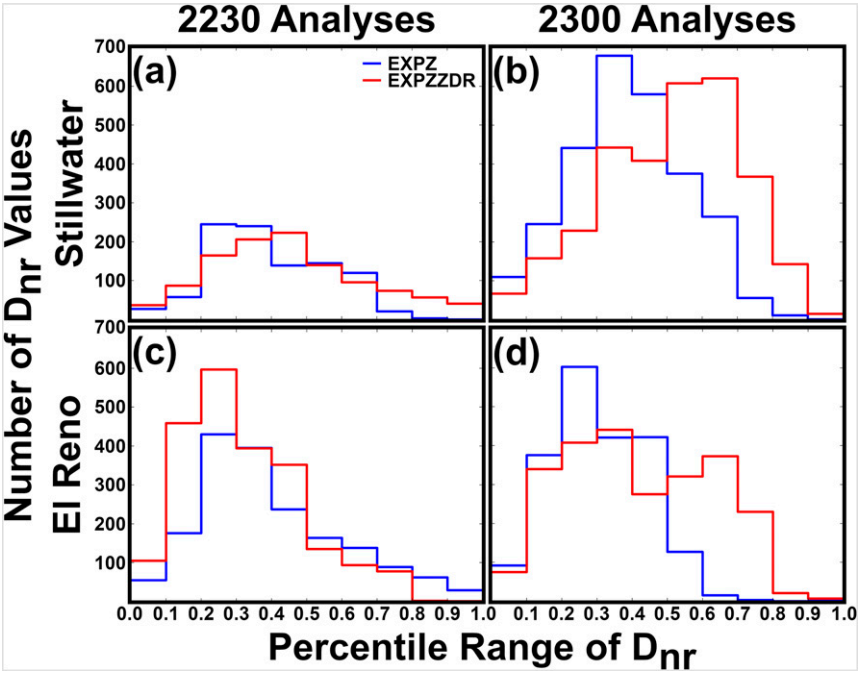

FIG. 14. Percentile histograms of rain mean mass diameter (D_{nr}, mm) for the Stillwater storm at the (a) 2230 and (b) 2300 UTC 31 May 2013 analyses and the El Reno storm at the (c) 2230 and (d) 2300 UTC analyses. The histograms cover all model grid points for the boxes in Fig. 13.

Improved forecasts of storms are possible with fewer DA cycles when those forecasts are initialized after several DA cycles that assimilate Z_{DR} observations during a window that captures the higher Z_{DR} values in the updraft and the microphysical state of storms that are initially developing and organizing.

There are several notable areas for future study. These initial tests provide insight on what improvements are seen in forecasts when assimilating Z_{DR} and that the most important times for DA cycles are during initial storm development and organization for the future assimilation of rapid-scan (~2 min) dual-pol PAR observations in a WoF-like system. Additionally, assimilating Z_{DR} during the early stages of storm organization improved analyzed updraft strength. A future study will look deeper into the correlation between the Z_{DR} observations and the microphysical and dynamical state variables to better determine how and where Z_{DR} observations have the greatest impact. The thresholds used for the Z_{DR} observation assimilation removed the potential for the Z_{DR} observations to correct any high bias in the background forecast DSDs. Future work must both further investigate the quality control of Z_{DR} observations to make assimilating noisy low Z_{DR} observations practical and assess how lower values impact the DSDs across the structure of convective storms in combination with the higher threshold values assimilated in this study. It is also noteworthy that the predicted storms exhibit little to no speed bias, which improves subsequent precipitation coverage compared to the observations. These results differ from other recent studies of similar supercell storms (Dawson et al. 2012; Yussouf et al. 2015; Snook et al. 2019), including the same case in Stratman et al. (2020). These studies used a different microphysics scheme and/or a different dynamic core. Understanding what modulates the storm propagation speed is a research topic that has relevance across multiple studies and is significant because forecasting the location of these supercells in the short term is critical to a successful WoF system. Future studies should also investigate the impact of assimilating additional polarimetric variables including specific differential phase (K_{DP}).

Acknowledgments. This research is funded by the Spectrum Efficient National Surveillance Radar (SENSR) program through NOAA/Office of Oceanic and Atmospheric Research under NOAA-University of Oklahoma Cooperative Agreement NA11OAR4320072, U.S. Department of Commerce. Authors Supinie, Xue, and Labriola were also supported by NOAA Grants NA16OAR4320115 and NA19OAR4590236. Kuster was also supported by NOAA Grant NA16OAR4320115. Most of the computing for this project was performed at the Texas Advanced Computing Center (TACC; http://www.tacc.utexas.edu) at the University of Texas at Austin. The authors thank Charles Kuster for providing the KOUN data, which were collected by researchers at the National Severe Storms Laboratory and are not publicly available (contact charles.kuster@noaa.gov). We would also like to thank the three anonymous reviewers whose thorough critiques contributed to a more complete and expansive manuscript.

Data availability statement. KTLX radar data can be accessed at https://www.ncdc.noaa.gov/nexradinv/chooseday.jsp?id=KTLX&Submit=Submit. Oklahoma Mesonet data can be accessed at

https://www.mesonet.org/index.php/weather/mesonet_data_files. ASOS/AWOS conventional observations can be accessed at ftp://ftp.ncdc.noaa.gov/pub/data/asos-fivemin/6401-2013/ and https://www.ncei.noaa.gov/access/search/data-search/global-hourly. GEFS, MRMS, and radiosonde data used for this project have been made available at https://dataverse.harvard.edu/dataverse/PJYSSXKL20.

REFERENCES

Aksoy, A., D. C. Dowell, and C. Snyder, 2009: A multicase comparative assessment of the ensemble Kalman filter for assimilation of radar observations. Part I: Storm-scale analyses. *Mon. Wea. Rev.*, **137**, 1805–1824, https://doi.org/10.1175/2008MWR2691.1.

Alexander, C., and Coauthors, 2020: Rapid Refresh (RAP) and High Resolution Rapid Refresh (HRRR) model development. *30th Conf. on Weather Analysis and Forecasting/26th Conf. on Numerical Weather Prediction*, Boston, MA, Amer. Meteor. Soc., 8C.1, https://ams.confex.com/ams/2020Annual/meetingapp.cgi/Paper/370205.

Balakrishnan, N., and D. S. Zrnić, 1990: Use of polarization to characterize precipitation and discriminate large hail. *J. Atmos. Sci.*, **47**, 1525–1540, https://doi.org/10.1175/1520-0469(1990)047<1525:UOPTCP>2.0.CO;2.

Benjamin, S. G., and Coauthors, 2016: A North American hourly assimilation and model forecast cycle: The Rapid Refresh. *Mon. Wea. Rev.*, **144**, 1669–1694, https://doi.org/10.1175/MWR-D-15-0242.1.

Brandes, E. A., J. Vivekanandan, J. D. Tuttle, and C. J. Kessinger, 1995: A study of thunderstorm microphysics with multiparameter radar and aircraft observations. *Mon. Wea. Rev.*, **123**, 3129–3143, https://doi.org/10.1175/1520-0493(1995)123<3129:ASOTMW>2.0.CO;2.

Bringi, V. N., and V. Chandrasekar, 2001: *Polarimetric Doppler Weather Radar*. Cambridge University Press, 636 pp.

Brock, F. V., K. C. Crawford, R. L. Elliott, G. W. Cuperus, S. J. Stadler, H. L. Johnson, and M. D. Eilts, 1995: The Oklahoma Mesonet: A technical overview. *J. Atmos. Oceanic Technol.*, **12**, 5–19, https://doi.org/10.1175/1520-0426(1995)012<0005:TOMATO>2.0.CO;2.

Brown, B. G., 2001: Verification of precipitation forecasts: A survey of methodology. Part II: Verification of probability forecasts at points. National Center for Atmospheric Research, 20 pp., https://cawcr.gov.au/projects/verification/QPF_Prague2001/papers/bgb_paper_final.pdf.

Bryan, G. H., J. C. Wyngaard, and J. M. Fritsch, 2003: Resolution requirements for the simulation of deep moist convection. *Mon. Wea. Rev.*, **131**, 2394–2416, https://doi.org/10.1175/1520-0493(2003)131<2394:RRFTSO>2.0.CO;2.

Carlin, J. T., J. Gao, J. C. Snyder, and A. V. Ryzhkov, 2017: Assimilation of ZDR columns for improving the spinup and forecast of convective storms in storm-scale models: Proof-of-concept experiments. *Mon. Wea. Rev.*, **145**, 5033–5057, https://doi.org/10.1175/MWR-D-17-0103.1.

Carr, N., P. E. Kirstetter, J. J. Gourley, and Y. Hong, 2017: Polarimetric signatures of midlatitude warm-rain precipitation events. *J. Appl. Meteor. Climatol.*, **56**, 697–711, https://doi.org/10.1175/JAMC-D-16-0164.1.

Carrió, D. S., V. Homar, and D. M. Wheatley, 2019: Potential of an EnKF storm-scale data assimilation system over sparse observation regions with complex orography. *Atmos. Res.*, **216**, 186–206, https://doi.org/10.1016/j.atmosres.2018.10.004.

Clark, A. J., and Coauthors, 2011: Probabilistic precipitation forecast skill as a function of ensemble size and spatial scale in a convection-allowing ensemble. *Mon. Wea. Rev.*, **139**, 1410–1418, https://doi.org/10.1175/2010MWR3624.1.

——, J. S. Kain, P. T. Marsh, J. Correia, M. Xue, and F. Kong, 2012: Forecasting tornado pathlengths using a three-dimensional object identification algorithm applied to convection-allowing forecasts. *Wea. Forecasting*, **27**, 1090–1113, https://doi.org/10.1175/WAF-D-11-00147.1.

——, J. Gao, P. T. Marsh, T. Smith, J. S. Kain, J. Correia, M. Xue, and F. Kong, 2013: Tornado pathlength forecasts from 2010 to 2011 using ensemble updraft helicity. *Wea. Forecasting*, **28**, 387–407, https://doi.org/10.1175/WAF-D-12-00038.1.

Dando, M. L., A. J. Thorpe, and J. R. Eyre, 2007: The optimal density of atmospheric sounder observations in the Met Office NWP system. *Quart. J. Roy. Meteor. Soc.*, **133**, 1933–1943, https://doi.org/10.1002/qj.175.

Dawson, D. T., II, M. Xue, J. A. Milbrandt, and M. K. Yau, 2010: Comparison of evaporation and cold pool development between single-moment and multimoment bulk microphysics schemes in idealized simulations of tornadic thunderstorms. *Mon. Wea. Rev.*, **138**, 1152–1171, https://doi.org/10.1175/2009MWR2956.1.

——, L. J. Wicker, E. R. Mansell, and R. L. Tanamachi, 2012: Impact of the environmental low-level wind profile on ensemble forecasts of the 4 May 2007 Greensburg, Kansas, tornadic storm and associated mesocyclones. *Mon. Wea. Rev.*, **140**, 696–716, https://doi.org/10.1175/MWR-D-11-00008.1.

——, ——, ——, Y. Jung, and M. Xue, 2013: Low-level polarimetric radar signatures in EnKF analyses and forecasts of the 8 May 2003 Oklahoma City tornadic supercell: Impact of multi-moment microphysics and comparisons with observations. *Adv. Meteor.*, **2013**, 818394, https://doi.org/10.1155/2013/818394.

——, E. R. Mansell, Y. Jung, L. J. Wicker, M. R. Kumjian, and M. Xue, 2014: Low-level Z_{DR} signatures in supercell forward flanks: The role of size sorting and melting of hail. *J. Atmos. Sci.*, **71**, 276–299, https://doi.org/10.1175/JAS-D-13-0118.1.

Dowell, D. C., and L. J. Wicker, 2009: Additive noise for storm-scale ensemble data assimilation. *J. Atmos. Oceanic Technol.*, **26**, 911–927, https://doi.org/10.1175/2008JTECHA1156.1.

——, ——, and C. Snyder, 2011: Ensemble Kalman filter assimilation of radar observations of the 8 May 2003 Oklahoma City supercell: Influences of reflectivity observations on storm-scale analyses. *Mon. Wea. Rev.*, **139**, 272–294, https://doi.org/10.1175/2010MWR3438.1.

Droegemeier, K. K., 1990: Toward a science of storm-scale prediction. Preprints, *16th Conf. on Severe Local Storms*, Kananaskis Park, AB, Canada, Amer. Meteor. Soc., 256–262.

Dudhia, J., 1989: Numerical study of convection observed during the Winter Monsoon Experiment using a mesoscale two-dimensional model. *J. Atmos. Sci.*, **46**, 3077–3107, https://doi.org/10.1175/1520-0469(1989)046<3077:NSOCOD>2.0.CO;2.

Ebert, E. E., 2001: Ability of a poor man's ensemble to predict the probability and distribution of precipitation. *Mon. Wea. Rev.*, **129**, 2461–2480, https://doi.org/10.1175/1520-0493(2001)129<2461:AOAPMS>2.0.CO;2.

Ehrendorfer, M., 1997: Predicting the uncertainty of numerical weather forecasts: A review. *Meteor. Z.*, **6**, 147–183, https://doi.org/10.1127/metz/6/1997/147.

Erickson, M. J., J. S. Kastman, B. Albright, S. Perfater, J. A. Nelson, R. S. Schumacher, and G. R. Herman, 2019: Verification results from the 2017 HMT–WPC Flash Flood and Intense Rainfall

Experiment. *J. Appl. Meteor. Climatol.*, **58**, 2591–2604, https://doi.org/10.1175/JAMC-D-19-0097.1.

Evans, C., D. F. Van Dyke, and T. Lericos, 2014: How do forecasters utilize output from a convection-permitting ensemble forecast system? Case study of a high-impact precipitation event. *Wea. Forecasting*, **29**, 466–486, https://doi.org/10.1175/WAF-D-13-00064.1.

Evensen, G., 1994: Sequential data assimilation with a nonlinear quasi-geostrophic model using Monte Carlo methods to forecast error statistics. *J. Geophys. Res.*, **99**, 10 143–10 162, https://doi.org/10.1029/94JC00572.

——, 2003: The ensemble Kalman filter: Theoretical formulation and practical implementation. *Ocean Dyn.*, **53**, 343–367, https://doi.org/10.1007/s10236-003-0036-9.

Fowler, A. M., S. L. Dance, and J. A. Waller, 2018: On the interaction of observation and prior error correlations in data assimilation. *Quart. J. Roy. Meteor. Soc.*, **144**, 48–62, https://doi.org/10.1002/qj.3183.

Gaspari, G., and S. E. Cohn, 1999: Construction of correlation functions in two and three dimensions. *Quart. J. Roy. Meteor. Soc.*, **125**, 723–757, https://doi.org/10.1002/qj.49712555417.

Gallo, B. T., A. J. Clark, and S. R. Dembek, 2016: Forecasting tornadoes using convection-permitting ensembles. *Wea. Forecasting*, **31**, 273–295, https://doi.org/10.1175/WAF-D-15-0134.1.

Grell, G. A., and D. Devenyi, 2002: A generalized approach to parameterizing convection combining ensemble and data assimilation techniques. *Geophys. Res. Lett.*, **29**, 1693, https://doi.org/10.1029/2002GL015311.

Hilton, F., A. Collard, V. Guidard, R. Randriamampianina, and M. Schwaerz, 2009: Assimilation of IASI radiances at European NWP centres. *Workshop on the Assimilation of IASI Data in NWP*, Reading, UK, ECMWF, 39–48, https://www.ecmwf.int/sites/default/files/elibrary/2009/9896-assimilation-iasi-radiances-european-nwp-centres.pdf.

Hong, S.-Y., Y. Noh, and J. Dudhia, 2006: A new vertical diffusion package with an explicit treatment of entrainment processes. *Mon. Wea. Rev.*, **134**, 2318–2341, https://doi.org/10.1175/MWR3199.1.

Houtekamer, P. L., and F. Zhang, 2016: Review of the ensemble Kalman filter for atmospheric data assimilation. *Mon. Wea. Rev.*, **144**, 4489–4532, https://doi.org/10.1175/MWR-D-15-0440.1.

——, X. Deng, H. L. Mitchell, S. Baek, and N. Gagnon, 2014: Higher resolution in an operational ensemble Kalman filter. *Mon. Wea. Rev.*, **142**, 1143–1162, https://doi.org/10.1175/MWR-D-13-00138.1.

Hu, M., H. Shao, D. Stark, K. Newman, and C. Zhou, 2015a: Gridpoint Statistical Interpolation (GSI) user's guide for version 3.4. Developmental Testbed Center, 143 pp., https://dtcenter.ucar.edu/com-GSI/users/docs/users_guide/GSIUserGuide_v3.4.pdf.

——, ——, ——, ——, and ——, 2015b: Ensemble Kalman Filter (EnKF) user's guide for version 1.0. Developmental Testbed Center, 82 pp., https://dtcenter.org/sites/default/files/community-code/enkf/docs/users-guide/EnKF_UserGuide_v1.0.pdf.

Hudson, D., 2017: Ensemble verification metrics. ECMWF Annual Seminar, Bureau of Meteorology, 39 pp., https://www.ecmwf.int/sites/default/files/elibrary/2017/17626-ensemble-verification-metrics.pdf.

Iacono, M. J., J. S. Delamere, E. J. Mlawer, M. W. Shephard, S. A. Clough, and W. D. Collins, 2008: Radiative forcing by long-lived greenhouse gases: Calculations with the AER radiative transfer models. *J. Geophys. Res.*, **113**, D13103, https://doi.org/10.1029/2008JD009944.

Iyer, E. R., A. J. Clark, M. Xue, and F. Kong, 2016: A comparison of 36–60-h precipitation forecasts from convection-allowing and convection-parameterizing ensembles. *Wea. Forecasting*, **31**, 647–661, https://doi.org/10.1175/WAF-D-15-0143.1.

Janjić, Z. I., 2002: Nonsingular implementation of the Mellor–Yamada level 2.5 scheme in the NCEP Meso model. NCEP Office Note 437, 61 pp., https://www.emc.ncep.noaa.gov/officenotes/newernotes/on437.pdf.

Johnson, M., Y. Jung, D. Dawson, and M. Xue, 2016: Comparison of simulated polarimetric signatures in idealized supercell storms using two-moment bulk microphysics schemes in WRF. *Mon. Wea. Rev.*, **144**, 971–996, https://doi.org/10.1175/MWR-D-15-0233.1.

——, ——, J. A. Milbrandt, H. Morrison, and M. Xue, 2019: Effects of the representation of rimed ice in bulk microphysics schemes on polarimetric signatures. *Mon. Wea. Rev.*, **147**, 3785–3810, https://doi.org/10.1175/MWR-D-18-0398.1.

Jung, Y., G. Zhang, and M. Xue, 2008a: Assimilation of simulated polarimetric radar data for a convective storm using ensemble Kalman filter. Part I: Observation operators for reflectivity and polarimetric variables. *Mon. Wea. Rev.*, **136**, 2228–2245, https://doi.org/10.1175/2007MWR2083.1.

——, M. Xue, G. Zhang, and J. Straka, 2008b: Assimilation of simulated polarimetric radar data for a convective storm using ensemble Kalman filter. Part II: Impact of polarimetric data on storm analysis. *Mon. Wea. Rev.*, **136**, 2246–2260, https://doi.org/10.1175/2007MWR2288.1.

——, ——, and ——, 2010: Simulations of polarimetric radar signatures of a supercell storm using a two-moment bulk microphysics scheme. *J. Appl. Meteor. Climatol.*, **49**, 146–163, https://doi.org/10.1175/2009JAMC2178.1.

——, ——, and M. Tong, 2012: Ensemble Kalman filter analyses of the 29-30 May 2004 Oklahoma tornadic thunderstorm using one- and two-moment bulk microphysics schemes, with verification against polarimetric radar data. *Mon. Wea. Rev.*, **140**, 1457–1475, https://doi.org/10.1175/MWR-D-11-00032.1.

Kain, J. S., 2004: The Kain–Fritsch convective parameterization: An update. *J. Appl. Meteor.*, **43**, 170–181, https://doi.org/10.1175/1520-0450(2004)043<0170:TKCPAU>2.0.CO;2.

——, and J. M. Fritsch, 1993: Convective parameterization for mesoscale models: The Kain–Fritsch scheme. *The Representation of Cumulus Convection in Numerical Models, Meteor. Monogr.*, No. 46, Amer. Meteor. Soc., 165–170, https://doi.org/10.1007/978-1-935704-13-3_16.

——, and Coauthors, 2008: Some practical considerations regarding horizontal resolution in the first generation of operational convection-allowing NWP. *Wea. Forecasting*, **23**, 931–952, https://doi.org/10.1175/WAF2007106.1.

Kingfield, D. M., and J. C. Picca, 2018: Development of an operational convective nowcasting algorithm using raindrop size sorting information from polarimetric radar data. *Wea. Forecasting*, **33**, 1477–1495, https://doi.org/10.1175/WAF-D-18-0025.1.

Kumjian, M., and A. V. Ryzhkov, 2008: Polarimetric signatures in supercell thunderstorms. *J. Appl. Meteor. Climatol.*, **47**, 1940–1961, https://doi.org/10.1175/2007JAMC1874.1.

Kumjian, M. R., A. P. Khain, N. Benmoshe, E. Ilotoviz, A. V. Ryzhkov, and V. T. J. Phillips, 2014: The anatomy and physics of ZDR columns: Investigating a polarimetric radar signature with a spectral bin microphysical model. *J. Appl. Meteor. Climatol.*, **53**, 1820–1843, https://doi.org/10.1175/JAMC-D-13-0354.1.

Kuster, C. M., P. L. Heinselman, J. C. Snyder, K. A. Wilson, D. A. Speheger, and J. E. Hocker, 2017: An evaluation of radar-based tornado track estimation products by Oklahoma public

safety officials. *Wea. Forecasting*, **32**, 1711–1726, https://doi.org/10.1175/WAF-D-17-0031.1.

——, J. C. Snyder, T. J. Schuur, T. T. Lindley, P. L. Heinselman, J. C. Furtado, J. W. Brogden, and R. Toomey, 2019: Rapid-update radar observations of Z_{DR} column depth and its use in the warning decision process. *Wea. Forecasting*, **34**, 1173–1188, https://doi.org/10.1175/WAF-D-19-0024.1.

Labriola, J., N. Snook, Y. Jung, and M. Xue, 2019a: Explicit ensemble prediction of hail in 19 May 2013 Oklahoma City thunderstorms and analysis of hail growth processes with several multimoment microphysics schemes. *Mon. Wea. Rev.*, **147**, 1193–1213, https://doi.org/10.1175/MWR-D-18-0266.1.

——, ——, M. Xue, and K. Thomas, 2019b: Forecasting the 8 May 2017 severe hail storm in Denver, Colorado, at a convection allowing resolution: Understanding rimed ice treatments in multimoment microphysics schemes and their effects on hail size forecasts. *Mon. Wea. Rev.*, **147**, 3045–3068, https://doi.org/10.1175/MWR-D-18-0319.1.

Lakshmanan, V., T. Smith, G. Stumpf, and K. Hondl, 2007: The Warning Decision Support System–Integrated Information. *Wea. Forecasting*, **22**, 596–612, https://doi.org/10.1175/WAF1009.1.

——, C. Karstens, J. Krause, and L. Tang, 2014: Quality control of weather radar data using polarimetric variables. *J. Atmos. Oceanic Technol.*, **31**, 1234–1249, https://doi.org/10.1175/JTECH-D-13-00073.1.

Lei, T., M. Xue, T. Y. Yu, and M. Teshiba, 2007: Study on the optimal scanning strategies of phase-array radar through ensemble Kalman filter assimilation of simulated data. *33rd Int. Conf. on Radar Meteorology*, Cairns, Australia, Amer. Meteor. Soc., P7.1, http://ams.confex.com/ams/pdfpapers/124022.pdf.

Li, X., and J. R. Mecikalski, 2010: Assimilation of the dual-polarization Doppler radar data for a convective storm with a warm-rain radar forward operator. *J. Geophys. Res.*, **115**, D16208, https://doi.org/10.1029/2009JD013666.

——, and ——, 2012: Impact of the dual-polarization Doppler radar data on two convective storms with a warm-rain radar forward operator. *Mon. Wea. Rev.*, **140**, 2147–2167, https://doi.org/10.1175/MWR-D-11-00090.1.

——, ——, and D. Posselt, 2017: An ice-phase microphysics forward model and preliminary results of polarimetric radar data assimilation. *Mon. Wea. Rev.*, **145**, 683–708, https://doi.org/10.1175/MWR-D-16-0035.1.

Lilly, D. K., 1990: Numerical prediction of thunderstorms—Has its time come? *Quart. J. Roy. Meteor. Soc.*, **116**, 779–798, https://doi.org/10.1002/QJ.49711649402.

Lim, K.-S. S., and S.-Y. Hong, 2010: Development of an effective double-moment cloud microphysics scheme with prognostic cloud condensation nuclei (CCN) for weather and climate models. *Mon. Wea. Rev.*, **138**, 1587–1612, https://doi.org/10.1175/2009MWR2968.1.

Lim, S., S. Allabakash, B. Jang, and V. Chandrasekar, 2018: Polarimetric radar signatures of a rare tornado event over South Korea. *J. Atmos. Oceanic Technol.*, **35**, 1977–1997, https://doi.org/10.1175/JTECH-D-18-0041.1.

Loeser, C. F., M. A. Herrera, and I. Szunyogh, 2017: An assessment of the performance of the operational global ensemble forecast systems in predicting the forecast uncertainty. *Wea. Forecasting*, **32**, 149–164, https://doi.org/10.1175/WAF-D-16-0126.1.

Loken, E. D., A. J. Clark, M. Xue, and F. Kong, 2017: Comparison of next-day probabilistic severe weather forecasts from coarse- and fine-resolution CAMs and a convection-allowing ensemble. *Wea. Forecasting*, **32**, 1403–1421, https://doi.org/10.1175/WAF-D-16-0200.1.

Loney, M. L., D. S. Zrnić, J. M. Straka, and A. V. Ryzhkov, 2002: Enhanced polarimetric radar signatures above the melting level in a supercell storm. *J. Appl. Meteor.*, **41**, 1179–1194, https://doi.org/10.1175/1520-0450(2002)041<1179:EPRSAT>2.0.CO;2.

Mansell, E. R., C. L. Ziegler, and E. C. Bruning, 2010: Simulated electrification of a small thunderstorm with two-moment bulk microphysics. *J. Atmos. Sci.*, **67**, 171–194, https://doi.org/10.1175/2009JAS2965.1.

Mason, I. B., 1982: A model for the assessment of weather forecasts. *Aust. Meteor. Mag.*, **30**, 291–303.

Mason, S. J., and N. E. Graham, 1999: Conditional probabilities, relative operating characteristics, and relative operating levels. *Wea. Forecasting*, **14**, 713–725, https://doi.org/10.1175/1520-0434(1999)014<0713:CPROCA>2.0.CO;2.

Matsui, T., B. Dolan, T. Iguchi, S. A. Rutledge, W. Tao, and S. Lang, 2020: Polarimetric radar characteristics of simulated and observed intense convective cores for a midlatitude continental and tropical maritime environment. *J. Hydrometeor.*, **21**, 501–517, https://doi.org/10.1175/JHM-D-19-0185.1.

McPherson, R. A., and Coauthors, 2007: Statewide monitoring of the mesoscale environment: A technical update on the Oklahoma Mesonet. *J. Atmos. Oceanic Technol.*, **24**, 301–321, https://doi.org/10.1175/JTECH1976.1.

Milbrandt, J. A., and M. K. Yau, 2005: A multimoment bulk microphysics parameterization. Part II: A proposed three-moment closure and scheme description. *J. Atmos. Sci.*, **62**, 3065–3081, https://doi.org/10.1175/JAS3535.1.

Mlawer, E. J., S. J. Taubman, P. D. Brown, M. J. Iacono, and S. A. Clough, 1997: Radiative transfer for inhomogeneous atmospheres: RRTM, a validated correlated-*k* model for the longwave. *J. Geophys. Res.*, **102**, 16 663–16 682, https://doi.org/10.1029/97JD00237.

Morrison, H., J. A. Curry, and V. I. Khvorostyanov, 2005: A new double-moment microphysics parameterization for application in cloud and climate models. Part I: Description. *J. Atmos. Sci.*, **62**, 1665–1677, https://doi.org/10.1175/JAS3446.1.

——, G. Thompson, and V. Tatarskii, 2009: Impact of cloud microphysics on the development of trailing stratiform precipitation in a simulated squall line: Comparison of one- and two-moment schemes. *Mon. Wea. Rev.*, **137**, 991–1007, https://doi.org/10.1175/2008MWR2556.1.

Nakanishi, M., and H. Niino, 2006: An improved Mellor–Yamada level 3 model: Its numerical stability and application to a regional prediction of advecting fog. *Bound.-Layer Meteor.*, **119**, 397–407, https://doi.org/10.1007/s10546-005-9030-8.

——, and ——, 2009: Development of an improved turbulence closure model for the atmospheric boundary layer. *J. Meteor. Soc. Japan*, **87**, 895–912, https://doi.org/10.2151/jmsj.87.895.

NOAA/NCEI, 1901a: Automated surface observing system. Subset used: 31 May 2013–1 June 2013, National Centers for Environmental Information Land-Based Station datasets and products, accessed 6 November 2017, ftp://ftp.ncdc.noaa.gov/pub/data/asos-fivemin/6401-2013/.

——, 1901b: Automated weather observing system. Subset used: 31 May 2013–1 June 2013, National Centers for Environmental Information Land-Based Station datasets and products, accessed 6 November 2017, https://www.ncei.noaa.gov/access/search/data-search/global-hourly.

——, 1905: Integrated global radiosonde archive. Subset used: 31 May 2013–1 June 2013, National Centers for Environmental Information Weather Balloon Data, accessed 6 November 2017, https://dataverse.harvard.edu/dataverse/PJYSSXKL20.

——, 1991: NEXRAD data archive. Subset used: 31 May 2013–1 June 2013, National Centers for Environmental Information Radar Data, accessed 21 July 2018, https://www.ncdc.noaa.gov/nexradinv/chooseday.jsp?id=KTLX&Submit=Submit.

NOAA/NCEP, 1992: Global Ensemble Forecast System. Subset used: 31 May 2013–1 June 2013, National Centers for Environmental Prediction Product Inventory—GEFS Products, accessed 31 May 2013, https://dataverse.harvard.edu/dataverse/PJYSSXKL20.

NOAA/NSSL, 2014: Merged Azimuthal Shear. Subset used: 31 May 2013–1 June 2013, Multi-Radar/Multi-Sensor System, accessed 1 May 2018, https://dataverse.harvard.edu/dataverse/PJYSSXKL20.

NWS, 2019: The May 31, 2013 El Reno, OK Tornado. NOAA, accessed 27 November 2019, https://www.weather.gov/oun/events-20130531-elreno.

Oklahoma Climatological Survey/Oklahoma Mesonet, 1994: Mesonet Data Files. Subset 31 May 2013–1 June 2013, Mesonet Past Data and Files, accessed 6 November 2017, https://www.mesonet.org/index.php/weather/mesonet_data_files.

Park, H. S., A. V. Ryzhkov, D. S. Zrnić, and K. Kim, 2009: The hydrometeor classification algorithm for the polarimetric WSR-88D: Description and application to an MCS. *Wea. Forecasting*, **24**, 730–748, https://doi.org/10.1175/2008WAF2222205.1.

Picca, J., and A. Ryzhkov, 2012: A dual-wavelength polarimetric analysis of the 16 May 2010 Oklahoma City extreme hailstorm. *Mon. Wea. Rev.*, **140**, 1385–1403, https://doi.org/10.1175/MWR-D-11-00112.1.

Putnam, B. J., M. Xue, Y. Jung, N. A. Snook, and G. Zhang, 2014: The analysis and prediction of microphysical states and polarimetric variables in a mesoscale convective system using double-moment microphysics, multinetwork radar data, and the ensemble Kalman filter. *Mon. Wea. Rev.*, **142**, 141–162, https://doi.org/10.1175/MWR-D-13-00042.1.

——, ——, ——, ——, and ——, 2017: Ensemble probabilistic prediction of a mesoscale convective system and associated polarimetric radar variables using single-moment and double-moment microphysics schemes and EnKF radar data assimilation. *Mon. Wea. Rev.*, **145**, 2257–2279, https://doi.org/10.1175/MWR-D-16-0162.1.

Putnam, B., M. Xue, Y. Jung, N. Snook, and G. Zhang, 2019: Ensemble Kalman filter assimilation of polarimetric radar observations for the 20 May 2013 Oklahoma tornadic supercell case. *Mon. Wea. Rev.*, **147**, 2511–2533, https://doi.org/10.1175/MWR-D-18-0251.1.

Radar Operations Center, 2013: WSR-88D dual polarization deployment progress. NOAA, 6 pp., https://www.roc.noaa.gov/WSR88D/PublicDocs/DualPol/Dpstatus.pdf.

Romine, G. S., C. S. Schwartz, J. Berner, K. Fossell, C. Snyder, J. L. Anderson, and M. L. Weisman, 2014: Representing forecast error in a convection-permitting ensemble system. *Mon. Wea. Rev.*, **142**, 4519–4541, https://doi.org/10.1175/MWR-D-14-00100.1.

Ryzhkov, A. V., T. J. Schuur, D. W. Burgess, P. L. Heinselman, S. E. Giangrande, and D. S. Zrnić, 2005: The Joint Polarization Experiment: Polarimetric rainfall measurements and hydrometeor classification. *Bull. Amer. Meteor. Soc.*, **86**, 809–824, https://doi.org/10.1175/BAMS-86-6-809.

Satterfield, E., and I. Szunyogh, 2010: Predictability of the performance of an ensemble forecast system: Predictability of the space of uncertainties. *Mon. Wea. Rev.*, **138**, 962–981, https://doi.org/10.1175/2009MWR3049.1.

Scharfenberg, K. A., and Coauthors, 2005: The Joint Polarization Experiment: Polarimetric radar in forecasting and warning decision making. *Wea. Forecasting*, **20**, 775–788, https://doi.org/10.1175/WAF881.1.

Sivillo, J. K., J. E. Ahlquist, and Z. Toth, 1997: An ensemble forecasting primer. *Wea. Forecasting*, **12**, 809–818, https://doi.org/10.1175/1520-0434(1997)012<0809:AEFP>2.0.CO;2.

Skamarock, W. C., and Coauthors, 2008: A description of the Advanced Research WRF version 3. NCAR Tech. Note NCAR/TN-475+STR, 113 pp., https://doi.org/10.5065/D68S4MVH.

Skinner, P. S., and Coauthors, 2018: Object-based verification of a prototype warn-on-forecast system. *Wea. Forecasting*, **33**, 1225–1250, https://doi.org/10.1175/WAF-D-18-0020.1.

Smith, T. M., K. L. Elmore, and S. A. Dulin, 2004: A damaging downburst prediction and detection algorithm for the WSR-88D. *Wea. Forecasting*, **19**, 240–250, https://doi.org/10.1175/1520-0434(2004)019<0240:ADDPAD>2.0.CO;2.

——, and Coauthors, 2016: Multi-Radar Multi-Sensor (MRMS) severe weather and aviation products: Initial operating capabilities. *Bull. Amer. Meteor. Soc.*, **97**, 1617–1630, https://doi.org/10.1175/BAMS-D-14-00173.1.

Snook, N., M. Xue, and Y. Jung, 2012: Ensemble probabilistic forecasts of a tornadic mesoscale convective system from ensemble Kalman filter analyses using WSR-88D and CASA radar data. *Mon. Wea. Rev.*, **140**, 2126–2146, https://doi.org/10.1175/MWR-D-11-00117.1.

——, ——, and ——, 2015: Multiscale EnKF assimilation of radar and conventional observations and ensemble forecasting for a tornadic mesoscale convective system. *Mon. Wea. Rev.*, **143**, 1035–1057, https://doi.org/10.1175/MWR-D-13-00262.1.

——, Y. Jung, J. Brotzge, B. Putnam, and M. Xue, 2016: Prediction and ensemble forecast verification of hail in the supercell storms of 20 May 2013. *Wea. Forecasting*, **31**, 811–825, https://doi.org/10.1175/WAF-D-15-0152.1.

——, M. Xue, and Y. Jung, 2019: Tornado-resolving ensemble and probabilistic predictions of the 20 May 2013 Newcastle–Moore EF5 tornado. *Mon. Wea. Rev.*, **147**, 1215–1235, https://doi.org/10.1175/MWR-D-18-0236.1.

Snyder, J. C., H. B. Bluestein, V. Venkatesh, and S. J. Frasier, 2013: Observations of polarimetric signatures in supercells by an X-band mobile doppler radar. *Mon. Wea. Rev.*, **141**, 3–29, https://doi.org/10.1175/MWR-D-12-00068.1.

Sobash, R. A., J. S. Kain, D. R. Bright, A. R. Dean, M. C. Coniglio, and S. J. Weiss, 2011: Probabilistic forecast guidance for severe thunderstorms based on the identification of extreme phenomena in convection-allowing model forecasts. *Wea. Forecasting*, **26**, 714–728, https://doi.org/10.1175/WAF-D-10-05046.1.

——, G. S. Romine, C. S. Schwartz, D. J. Gagne, and M. L. Weisman, 2016: Explicit forecasts of low-level rotation from convection-allowing models for next-day tornado prediction. *Wea. Forecasting*, **31**, 1591–1614, https://doi.org/10.1175/WAF-D-16-0073.1.

SPC, 2019: SPC storm archive for 5/31/2013, accessed 27 November 2019, https://www.spc.noaa.gov/exper/archive/event.php?date=20130531.

Starzec, M., C. R. Homeyer, and G. L. Mullendore, 2017: Storm labeling in three dimensions (SL3D): A volumetric radar echo and dual-polarization updraft classification algorithm. *Mon. Wea. Rev.*, **145**, 1127–1145, https://doi.org/10.1175/MWR-D-16-0089.1.

Stensrud, D. J., and Coauthors, 2009: Convective-scale warn-on-forecast system. *Bull. Amer. Meteor. Soc.*, **90**, 1487–1500, https://doi.org/10.1175/2009BAMS2795.1.

——, and Coauthors, 2013: Progress and challenges with warn-on-forecast. *Atmos. Res.*, **123**, 2–16, https://doi.org/10.1016/j.atmosres.2012.04.004.

Stratman, D. R., N. Yussouf, Y. Jung, T. A. Supinie, M. Xue, P. S. Skinner, and B. J. Putnam, 2020: Optimal temporal frequency of NSSL phased-array radar observations for an experimental warn-on-forecast system. *Wea. Forecasting*, **35**, 193–214, https://doi.org/10.1175/WAF-D-19-0165.1.

Supinie, T. A., N. Yussouf, J. Cheng, Y. Jung, M. Xue, and S. Wang, 2017: Comparison of the analyses and forecasts of a tornadic supercell storm from assimilating phased array radar and WSR-88D observations. *Wea. Forecasting*, **32**, 1379–1401, https://doi.org/10.1175/WAF-D-16-0159.1.

Tanamachi, R. L., and P. L. Heinselman, 2016: Rapid-scan, polarimetric observations of central Oklahoma severe storms on 31 May 2013. *Wea. Forecasting*, **31**, 19–42, https://doi.org/10.1175/WAF-D-15-0111.1.

Tewari, M., and Coauthors, 2004: Implementation and verification of the unified Noah land surface model in the WRF Model. *20th Conf. on Weather Analysis and Forecasting/16th Conf. on Numerical Weather Prediction*, Seattle, WA, Amer. Meteor. Soc., 14A.2, https://ams.confex.com/ams/pdfpapers/69061.pdf.

Thompson, G., P. R. Field, R. M. Rasmussen, and W. D. Hall, 2008: Explicit forecasts of winter precipitation using an improved bulk microphysics scheme. Part II: Implementation of a new snow parameterization. *Mon. Wea. Rev.*, **136**, 5095–5115, https://doi.org/10.1175/2008MWR2387.1.

——, S. Tessendorf, A. Heymsfield, and I. Kyoko, 2018: Improving graupel and hail treatment in the Thompson microphysics parameterization. *North American Hail Workshop*, Boulder, CO, NCAR, P5.7, https://www.mmm.ucar.edu/north-american-hail-workshop.

Tiedtke, M., 1989: A comprehensive mass flux scheme for cumulus parameterization in large-scale models. *Mon. Wea. Rev.*, **117**, 1779–1800, https://doi.org/10.1175/1520-0493(1989)117<1779:ACMFSF>2.0.CO;2.

Tong, M., and M. Xue, 2005: Ensemble Kalman filter assimilation of Doppler radar data with a compressible nonhydrostatic model: OSSE experiments. *Mon. Wea. Rev.*, **133**, 1789–1807, https://doi.org/10.1175/MWR2898.1.

Toth, Z., Y. Zhu, and T. Marchok, 2001: The use of ensembles to identify forecasts with small and large uncertainty. *Wea. Forecasting*, **16**, 463–477, https://doi.org/10.1175/1520-0434(2001)016<0463:TUOETI>2.0.CO;2.

——, ——, and R. Wobus, 2004: March 2004 upgrades of the NCEP global ensemble forecast system. NOAA/NCEP/EMC, accessed 11 November 2019, https://www.emc.ncep.noaa.gov/gmb/ens/ens_imp_news.html.

Van Den Broeke, M. S., 2017: Polarimetric radar metrics related to tornado life cycles and intensity in supercell storms. *Mon. Wea. Rev.*, **145**, 3671–3686, https://doi.org/10.1175/MWR-D-16-0453.1.

——, 2020: A preliminary polarimetric radar comparison of pretornadic and nontornadic supercell storms. *Mon. Wea. Rev.*, **148**, 1567–1584, https://doi.org/10.1175/MWR-D-19-0296.1.

——, J. M. Straka, and E. N. Rasmussen, 2008: Polarimetric radar observations at low levels during tornado life cycles in a small sample of classic southern plains supercells. *J. Appl. Meteor. Climatol.*, **47**, 1232–1247, https://doi.org/10.1175/2007JAMC1714.1.

Wang, Y., Y. Jung, T. A. Supinie, and M. Xue, 2013: A hybrid MPI–OpenMP parallel algorithm and performance analysis for an ensemble square root filter suitable for dense observations. *J. Atmos. Oceanic Technol.*, **30**, 1382–1397, https://doi.org/10.1175/JTECH-D-12-00165.1.

Weber, M. E., J. Y. N. Cho, and H. G. Thomas, 2017: Command and control for multifunction phased array radar. *IEEE Trans. Geosci. Remote Sens.*, **55**, 5899–5912, https://doi.org/10.1109/TGRS.2017.2716935.

Wei, M., Z. Toth, R. Wobus, and Y. Zhu, 2008: Initial perturbations based on the ensemble transform (ET) technique in the NCEP global operational forecast system. *Tellus*, **60A**, 62–79, https://doi.org/10.1111/j.1600-0870.2007.00273.x.

Wheatley, D. M., N. Yussouf, and D. J. Stensrud, 2014: Ensemble Kalman filter analyses and forecasts of a severe mesoscale convective system using different choices of microphysics schemes. *Mon. Wea. Rev.*, **142**, 3243–3263, https://doi.org/10.1175/MWR-D-13-00260.1.

——, K. H. Knopfmeier, T. A. Jones, and G. J. Creager, 2015: Storm-scale data assimilation and ensemble forecasting with the NSSL Experimental Warn-on-Forecast System. Part I: Radar data experiments. *Wea. Forecasting*, **30**, 1795–1817, https://doi.org/10.1175/WAF-D-15-0043.1.

Whitaker, J. S., and T. M. Hamill, 2002: Ensemble data assimilation without perturbed observations. *Mon. Wea. Rev.*, **130**, 1913–1924, https://doi.org/10.1175/1520-0493(2002)130<1913:EDAWPO>2.0.CO;2.

——, and ——, 2012: Evaluating methods to account for system errors in ensemble data assimilation. *Mon. Wea. Rev.*, **140**, 3078–3089, https://doi.org/10.1175/MWR-D-11-00276.1.

Wu, B., J. Verlinde, and J. Sun, 2000: Dynamical and microphysical retrievals from Doppler radar observations of a deep convective cloud. *J. Atmos. Sci.*, **57**, 262–283, https://doi.org/10.1175/1520-0469(2000)057<0262:DAMRFD>2.0.CO;2.

Wu, C., L. Liu, X. Liu, G. Li, and C. Chen, 2018: Advances in Chinese dual-polarization and phased-array weather radars: Observational analysis of a supercell in southern China. *J. Atmos. Oceanic Technol.*, **35**, 1785–1806, https://doi.org/10.1175/JTECH-D-17-0078.1.

Xue, M., M. Tong, and K. K. Droegemeier, 2006: An OSSE framework based on the ensemble square-root Kalman filter for evaluating impact of data from radar networks on thunderstorm analysis and forecast. *J. Atmos. Oceanic Technol.*, **23**, 46–66, https://doi.org/10.1175/JTECH1835.1.

Yokohata, T., J. D. Annan, M. Collins, C. S. Jackson, M. Tobis, M. J. Webb, and J. C. Hargreaves, 2012: Reliability of multimodel and structurally different single-model ensembles. *Climate Dyn.*, **39**, 599–616, https://doi.org/10.1007/s00382-011-1203-1.

Yokota, S., H. Seko, M. Kunii, H. Yamauchi, and H. Niino, 2016: The tornadic supercell on the Kanto Plain on 6 May 2012: Polarimetric radar and surface data assimilation with EnKF and ensemble-based sensitivity analysis. *Mon. Wea. Rev.*, **144**, 3133–3157, https://doi.org/10.1175/MWR-D-15-0365.1.

Yussouf, N., and D. J. Stensrud, 2010: Impact of phased-array radar observations over a short assimilation period: Observing system simulation experiments using an ensemble Kalman filter. *Mon. Wea. Rev.*, **138**, 517–538, https://doi.org/10.1175/2009MWR2925.1.

——, E. R. Mansell, L. J. Wicker, D. M. Wheatley, and D. J. Stensrud, 2013: The ensemble Kalman filter analyses and forecasts of the 8 May 2003 Oklahoma City tornadic supercell storm using single- and double-moment microphysics

schemes. *Mon. Wea. Rev.*, **141**, 3388–3412, https://doi.org/10.1175/MWR-D-12-00237.1.

——, D. C. Dowell, L. J. Wicker, K. H. Knopfmeier, and D. M. Wheatley, 2015: Storm-scale data assimilation and ensemble forecasts for the 27 April 2011 severe weather outbreak in Alabama. *Mon. Wea. Rev.*, **143**, 3044–3066, https://doi.org/10.1175/MWR-D-14-00268.1.

——, J. S. Kain, and A. J. Clark, 2016: Short-term probabilistic forecasts of the 31 May 2013 Oklahoma tornado and flash flood event using a continuous-update-cycle storm-scale ensemble system. *Wea. Forecasting*, **31**, 957–983, https://doi.org/10.1175/WAF-D-15-0160.1.

Zhang, C., Y. Wang, and K. Hamilton, 2011: Improved representation of boundary layer clouds over the southeast Pacific in ARW-WRF using a modified Tiedtke cumulus parameterization scheme. *Mon. Wea. Rev.*, **139**, 3489–3513, https://doi.org/10.1175/MWR-D-10-05091.1.

Zhu, K., M. Xue, K. Ouyan, and Y. Jung, 2020: Assimilating polarimetric radar data with an ensemble Kalman filter: OSSEs with a tornadic supercell storm simulated with a two-moment microphysics scheme. *Quart. J. Roy. Meteor. Soc.*, **146**, 1880–1900, https://doi.org/10.1002/qj.3772.

Zrnić, D. S., and A. V. Ryzhkov, 1999: Polarimetry for weather surveillance radars. *Bull. Amer. Meteor. Soc.*, **80**, 389–406, https://doi.org/10.1175/1520-0477(1999)080<0389:PFWSR>2.0.CO;2.

——, V. N. Bringi, K. Aydin, N. Balakrishnan, V. Chandrasekar, and J. Hubbert, 1993: Polarimetric measurements in a severe hailstorm. *Mon. Wea. Rev.*, **121**, 2221–2238, https://doi.org/10.1175/1520-0493(1993)121<2223:PMIASH>2.0.CO;2.